

On the porous continuum-scale modeling of gravity-driven fingers in unsaturated materials: Numerical solution of a hypodiffusive governing equation that incorporates a hold-back-pile-up effect

Mehdi Eliassi and Robert J. Glass

Flow Visualization and Processes Laboratory, Sandia National Laboratories, Albuquerque, New Mexico, USA

Received 20 June 2002; revised 4 November 2002; accepted 13 March 2003; published 26 June 2003.

[1] We consider the use of a hypodiffusive governing equation (HDE) for the porous-continuum modeling of gravity-driven fingers (GDF) as occur in initially dry, highly nonlinear, and hysteretic porous media. In addition to the capillary and gravity terms within the traditional Richards equation, the HDE contains a hypodiffusive term that models an experimentally observed hold-back-pile-up (HBPU) effect and thus imparts nonmonotonicity at the wetting front. In its dimensionless form the HDE contains the dimensionless hypodiffusion number, N_{HD} . As N_{HD} increases, one-dimensional (1D) numerical solutions transition from monotonic to nonmonotonic. Considering the experimentally observed controls on GDF occurrence, as either the initial moisture content and applied flux increase or the material nonlinearity decreases, solutions undergo the required transition back to monotonic. Additional tests for horizontal imbibition and capillary rise show the HDE to yield the required monotonic response but display sharper fronts for $N_{HD} > 0$. Finally, two-dimensional (2D) numerical solutions illustrate that in parameter space where the 1D HDE yields nonmonotonicity, in 2D it forms nonmonotonic GDF. **INDEX TERMS:** 1829 Hydrology: Groundwater hydrology; 1875 Hydrology: Unsaturated zone; 1866 Hydrology: Soil moisture; **KEYWORDS:** capillary hysteresis, wetting front instability, preferential flow, extended irreversible thermodynamics, extended Darcy-Buckingham relations, hyperbolic and Navier-Stokes flux equations

Citation: Eliassi, M., and R. J. Glass, On the porous continuum-scale modeling of gravity-driven fingers in unsaturated materials: Numerical solution of a hypodiffusive governing equation that incorporates a hold-back-pile-up effect, *Water Resour. Res.*, 39(6), 1167, doi:10.1029/2002WR001535, 2003.

1. Introduction

[2] Gravity-driven fingering has been of interest for many years as a mechanism for preferential flow within the vadose zone. Extensive experimental and theoretical study (see the over 50 references listed by *Eliassi and Glass* [2002]) has elucidated much about the phenomenon. Interestingly, it has been found that individual gravity-driven fingers (GDF) exhibit nonmonotonicity in both pressure and saturation [*Glass et al.*, 1989; *Selker et al.*, 1992]. In combination with capillary hysteresis, this nonmonotonic behavior where finger tips are found to saturate (or nearly so) and then drain a distance behind, has been used to explain why fingers form a core and fringe zone structure that persists in time and from one infiltration cycle to another [*Glass et al.*, 1989]. In fact, it has been noted that from the time of initial finger formation onward, system behavior is controlled primarily by hysteresis-induced heterogeneity [*Glass and Nicholl*, 1996]. However, the critical behavior that is first required and from which the rest unfolds is an “overpressurization” or “kick” at the wetting front (WF) with a consequential “oversaturation.” This behavior has yet to be explained in context of a porous-continuum based unsaturated flow theory or included in

porous-continuum approaches for purposes of numerical simulation.

[3] The incorporation of the “kick” in numerical modeling of GDF has been shown to be essential. Recent attempts to numerically simulate GDF, using the traditional unsaturated flow theory represented by the Richards equation (RE) with standard monotonic hydraulic properties (i.e., hysteretic pressure-saturation and permeability-saturation functions [e.g., *van Genuchten*, 1980; *Mualem*, 1976]), required a numerical artifact to give the appropriate “kick” [*Eliassi and Glass*, 2001a]. In a set of artifact free simulations presented there we showed that even when a significant perturbation is imposed via a constant flux source the width of a finger at the top of a two-dimensional (2D) domain, solutions of the RE with standard monotonic properties (measured for materials that support GDF), yield a diffuse, monotonic plume and not nonmonotonic GDF. Even with the imposition of the traditional, highly nonlinear properties to create wetting fronts in homogeneous materials, as long as the properties remain monotonic, so do the solutions for constant flux boundary conditions. Thus without the “kick”, nonmonotonicity is not possible, diffusive behavior prevails, and GDF does not occur.

[4] To consider the extension of the standard porous-continuum approach to allow the modeling of GDF, in the work of *Eliassi and Glass* [2002] we identified the “kick” at the WF with the experimentally observed hold-back-pile-

up (HBPU) effect, where the hold back (HB) operates at the forward edge of the WF to prevent overspreading from capillary diffusion and the pile-up (PU) operates at the back of the WF to increase the pressure and thus the saturation of a finger tip. In combination with capillary hysteresis, the HBPU effect should lead to a pressure reversal immediately behind the WF to ultimately yield a nonmonotonic signature such as found in GDF. We incorporated the HBPU effect as an additional term within the porous-continuum governing equation for flow through unsaturated media, thus extending the traditional RE. Because experimental data suggests that the HBPU effect should be dependent on WF sharpness, we modeled the HBPU to be a simple function of the state variables (i.e., pressure and/or hysteretic moisture content). By induction, we postulated the HBPU effect in three different mathematical forms referred to as the hypodiffusive, $R_{hdiff}(\theta)$, hyperbolic, $R_{hyper}(\theta)$, and mixed, $R_{mix}(\theta)$, forms involving second and higher order spatial-temporal derivatives of the hysteretic moisture content as:

$$R_{hdiff}(\theta) = \vec{\nabla} \cdot [F(\theta)\vec{\nabla}\theta(\psi)] \quad (1)$$

$$R_{hyper}(\theta) = -\frac{\partial}{\partial t} \left[T(\theta) \frac{\partial}{\partial t} \theta(\psi) \right] \quad (2)$$

$$R_{mix}(\theta) = \vec{\nabla} \cdot \left\{ L(\theta) \vec{\nabla} \left[\frac{\partial}{\partial t} \theta(\psi) \right] \right\} \quad (3)$$

where $\vec{\nabla}$ [L^{-1}] is the gradient operator vector, $\theta(\psi)$ [L^3L^{-3}] is the hysteretic volumetric moisture content relation (i.e., the equation of state), ψ [L] is the capillary pressure head, t [T] is time, and functions $F(\theta)$ [L^2T^{-1}], $T(\theta)$ [T], and $L(\theta)$ [L^2] are new constitutive properties within each form of the HBPU effect.

[5] As presented by *Eliassi and Glass* [2002], all three formulations for $R(\theta)$ above, and their associated flux relations, have support in different extended theories for single- and multiphase flow found in the literature. A hypodiffusive flux relation can be distilled from the generalized two-phase flow theory of *Gray and Hassanizadeh* [1991] considering the concept of the Helmholtz free energy of the water-phase as influenced by phase interfaces. Within the context of extended irreversible thermodynamics, *del Rio and Lopez de Haro* [1991] derive a hyperbolic flux relation containing an inertial-like term with a relaxation time function that imparts memory. Simplification of the standard form of the Navier-Stokes equation also yields a hyperbolic flux relation. Finally, using the dynamic capillary pressure concept of *Gray and Hassanizadeh* [1991], where the capillary pressure is comprised of both static and time-dependent portions, a mixed-form flux can be derived.

[6] While the basic behavior of each form of $R(\theta)$, given in (1) to (3), can be verified analytically [*Eliassi and Glass*, 2002], numerical solution is required to consider whether any of these forms can yield the appropriate nonmonotonicity and GDF. Toward this end, the choice of which form to include in an extended governing equation remains arbitrary. As yet, none have been solved numerically to serve as a guide, each has different and equally plausible theoretical foundation, and all are formulated similarly to

depend on WF sharpness through spatial and temporal derivatives of the state variable. In this paper, we consider the numerical solution to a hypodiffusive governing equation (HDE) chosen simply because it does not contain additional derivatives in time and thus does not require special numerical techniques beyond those currently used to solve RE. We focus on one-dimensional (1D) solutions as a necessary first step given the highly nonlinear nature of the HDE. Our results confirm that the HBPU as incorporated in the HDE yields a nonmonotonic response that tracks experimental trends in GDF behavior with variation of initial moisture, applied flux, and material nonlinearity. Finally, we illustrate that nonmonotonicity in 1D modeled with a HBPU effect, indeed yields two-dimensional (2D) nonmonotonic GDF.

2. Theory

[7] In the work of *Eliassi and Glass* [2002], we postulated an extended hypodiffusive (HD) flux relation as an alternative porous continuum-scale representation of the flux in unsaturated porous materials. The HD flux is composed of two parts, the first being the traditional Darcy-Buckingham flux that includes capillary and gravitational drives and the second being due to the HBPU effect. The mathematical form of the hypodiffusive flux relation can be stated as:

$$\vec{q} = - \left[K(\theta) (\vec{\nabla}\psi + 1) + F(\theta) \vec{\nabla}\theta(\psi) \right] \quad (4)$$

where \vec{q} [LT^{-1}] is the flux vector, $K(\theta)$ [LT^{-1}] is the hydraulic conductivity function, and $F(\theta)$ [L^2T^{-1}] is the hypodiffusion function. To yield the HBPU effect, the hypodiffusion function must be such that as the WF is crossed, $F(\theta) \leq 0$.

[8] Assuming the continuity equation retains its standard form:

$$\frac{\partial}{\partial t} \theta(\psi) = -\vec{\nabla} \cdot \vec{q} \quad (5)$$

we can directly substitute (4) into (5) to obtain the associated governing equation as:

$$\left(\frac{\partial \theta(\psi)}{\partial \psi} \right) \frac{\partial \psi}{\partial t} = \vec{\nabla} \cdot \left[K(\theta) \vec{\nabla} \psi \right] + \delta \frac{\partial K(\theta)}{\partial z} + \vec{\nabla} \cdot \left[F(\theta) \vec{\nabla} \theta(\psi) \right] \quad (6)$$

where the derivative of $\theta(\psi)$ with respect to ψ is often referred to as the water capacity function, δ is a dimensionless constant that allows us to flexibly study the behavior of (6) under the influence of gravity (i.e., $\delta = 1$) as well as when gravity is absent (i.e., $\delta = 0$), and z [L] is the vertical direction. Here we refer to equation (6) as the hypodiffusive governing equation (HDE) with the last term on the right-hand side (RHS) of (6) being the hypodiffusive term, or $R_{hdiff}(\theta)$ in (1), where as $F(\theta) \rightarrow 0$, (6) reduces to the standard form of the RE.

[9] As (6) indicates, we must provide functional relationships for the hysteretic equation of state, $\theta(\psi)$, constitutive relation, $K(\theta)$, and the hypodiffusion function, $F(\theta)$. We represent the normalized forms of $\theta(\psi)$ and $K(\theta)$, using the

standard models of *van Genuchten* [1980] and *Mualem* [1976], respectively, as:

$$\Theta(\psi) \equiv \frac{\theta(\psi) - \theta_r}{\theta_s - \theta_r} = [1 + (\alpha|\psi|)^n]^{-m} \quad (7a)$$

$$\kappa(\Theta) \equiv \frac{K(\theta)}{K_s} = \sqrt{\Theta(\psi)} \left[1 - \left(1 - \Theta(\psi)^{1/m} \right)^m \right]^2 \quad (7b)$$

where $\Theta(\psi)$ refers to the hysteretic saturation function, θ_r [L^3L^{-3}] and θ_s [L^3L^{-3}] are respectively the residual and saturated (or satiated) moisture content values, α [L^{-1}] is the inverse capillary length, n defines the nonlinearity of the porous media, $m = 1 - (1/n)$, $\kappa(\Theta)$ is the normalized hydraulic conductivity function, and K_s [LT^{-1}] is the saturated conductivity of the medium. For brevity, the formulation we use for hysteresis in context of (7a) is presented in section 2.1, after we have nondimensionalized our equations.

[10] To consider the ability of the HDE to simulate nonmonotonicity, the precise formulation of $F(\theta)$ remains arbitrary as long as $F(\theta) \leq 0$ as the WF is crossed. In preliminary studies, we considered a variety of simple functional forms of $F(\theta)$ (e.g., monotonically decreasing, monotonically increasing, convex and concave forms, as well as constant), each giving qualitatively similar results. However, *Eliassi and Glass* [2002] showed that a parallel for the hypodiffusive flux can be found in the theory of Hassanizadeh and Gray (HG) [e.g., *Gray and Hassanizadeh*, 1991; *Hassanizadeh and Gray*, 1993a, 1993b]. While we do not know yet if this theory properly accounts for the underlying physics of the HBPU effect, we choose here to loosely ground $F(\theta)$ in the context of HG theory. Thus, as future measurements of fundamental quantities within the context of this theory are made, direct comparison to our simulations will allow judgment as to its appropriateness to model the HBPU. *Eliassi and Glass* [2002] found the HG theory to suggest for $F(\theta)$:

$$F(\theta) = \left(\frac{K(\theta)}{g} \right) \frac{\partial A^w(\theta)}{\partial \theta} \quad (8)$$

where g [LT^{-2}] is the acceleration of gravity, and $A^w(\theta)$ [L^2T^{-2}] is the macroscopic Helmholtz free energy per unit mass of the water phase as a function of water content [e.g., see *Hassanizadeh and Gray*, 1993a, 1993b]. To our knowledge, the functional form of $A^w(\theta)$ has yet to be measured or parameterized for unsaturated materials. Here we simply consider the following normalized form:

$$\Lambda(\Theta) \equiv \frac{A^w(\theta) - A_{\min}}{A_{\max} - A_{\min}} = 1 - [\Theta(\psi)]^b \quad (9)$$

where $\Lambda(\Theta)$ is the normalized free energy as a function of saturation, A_{\max} [L^2/T^2] and A_{\min} [L^2/T^2] refer to the minimum and maximum free energy values, respectively, and b is a positive exponent we take as 0.1 representing a mid range nonlinearity in (9). In (9), the free energy of water is assumed greatest (i.e., A_{\max}) at zero saturation, and then monotonically decreases as the saturation increases to a minimum (i.e., A_{\min}) at full saturation (or satiation). This behavior is consistent with the hypothesis of *Hassanizadeh*

and *Gray* [1993b], the primary physical basis for which is the replacement of air-solid interfaces with water-solid interfaces (heat of wetting). In addition, the functional form of the free energy is likely to be hysteretic because on drainage, a film of water is left behind on the solid in water wettable media. In fact, we found in preliminary attempts where $\Lambda(\Theta)$ is nonhysteretic, multiple nonmonotonicities, or pulsation, can occur along the profile [*Eliassi*, 2001]. Such pulsation is common when a nonwetting fluid displaces a wetting [e.g., *Glass et al.*, 2000] but not for wetting fluid invasion as we consider here. On the basis of these results and the physical justification that a water film is left behind on drainage, we simply assume that once a reversal to drainage takes place, $\Lambda(\Theta)$ remains constant.

2.1. Dimensionless Forms of the HDE and Constitutive Relations

[11] To simplify our studies, we nondimensionalize (6) by introducing the following dimensionless variables: $\Psi = \psi \alpha_{PWC}$, $\tau = t(\alpha_{PWC} K_s)$, $\vec{\nabla}^* = \vec{\nabla} / \alpha_{PWC}$, $\xi = z \alpha_{PWC}$, where Ψ , τ , $\vec{\nabla}^*$, and ξ represent the dimensionless pressure head, time, gradient operator, hydraulic conductivity function, and vertical position, respectively, and α_{PWC} [L^{-1}] is the inverse capillary length of the primary wetting curve (PWC). Following the substitution of these dimensionless variables into (6) and using the form of hypodiffusion function in (8), we have:

$$\left(\frac{\partial \Theta(\Psi)}{\partial \Psi} \right) \frac{\partial \Psi}{\partial \tau} = \vec{\nabla}^* \cdot \left[\kappa(\Theta) \vec{\nabla}^* \Psi \right] + \delta \frac{\partial \kappa(\Theta)}{\partial \xi} + N_{HD} \vec{\nabla}^* \cdot \left[\left(\kappa(\Theta) \frac{\partial \Lambda(\Theta)}{\partial \Theta} \right) \vec{\nabla}^* \Theta(\Psi) \right] \quad (10)$$

where N_{HD} is a new dimensionless group that we will call the hypodiffusion number:

$$N_{HD} = \frac{\alpha_{PWC}}{g} (A_{\max} - A_{\min}) \quad (11)$$

From (7) and (9) the dimensionless forms of the equation of state, constitutive relations, and free energy, respectively, are:

$$\Theta(\Psi) = [1 + (\alpha^* |\Psi|)^n]^{-m} \quad (12a)$$

$$\kappa(\Theta) = \sqrt{\Theta(\Psi)} \left[1 - \left(1 - \Theta(\Psi)^{1/m} \right)^m \right]^2 \quad (12b)$$

$$\Lambda(\Theta) = 1 - [\Theta(\Psi)]^b \quad (12c)$$

where $\alpha^* = \alpha_c / \alpha_{PWC}$ is the dimensionless inverse capillary length for a given hysteretic saturation branch c . We use the variable α_H^* to define the maximum hysteresis loop size given as the ratio of α_{MDC} to α_{PWC} , where α_{MDC} [L^{-1}] is the inverse capillary length for the main drainage curve (MDC) [see *Eliassi and Glass*, 2001a]. To illustrate the functional variations of hysteretic $\Theta(\Psi)$ and $\kappa(\Theta)$, Figures 1a and 1b, respectively, show the typical bounding hysteresis loops and permeability curves for $n = 2$ and $n = 15$, which represent the bounding n values considered in this paper. Here we have used (12a) with $\alpha^* = 1$ and $\alpha^* = 0.5$ (yielding $\alpha_H^* = 0.5$) to

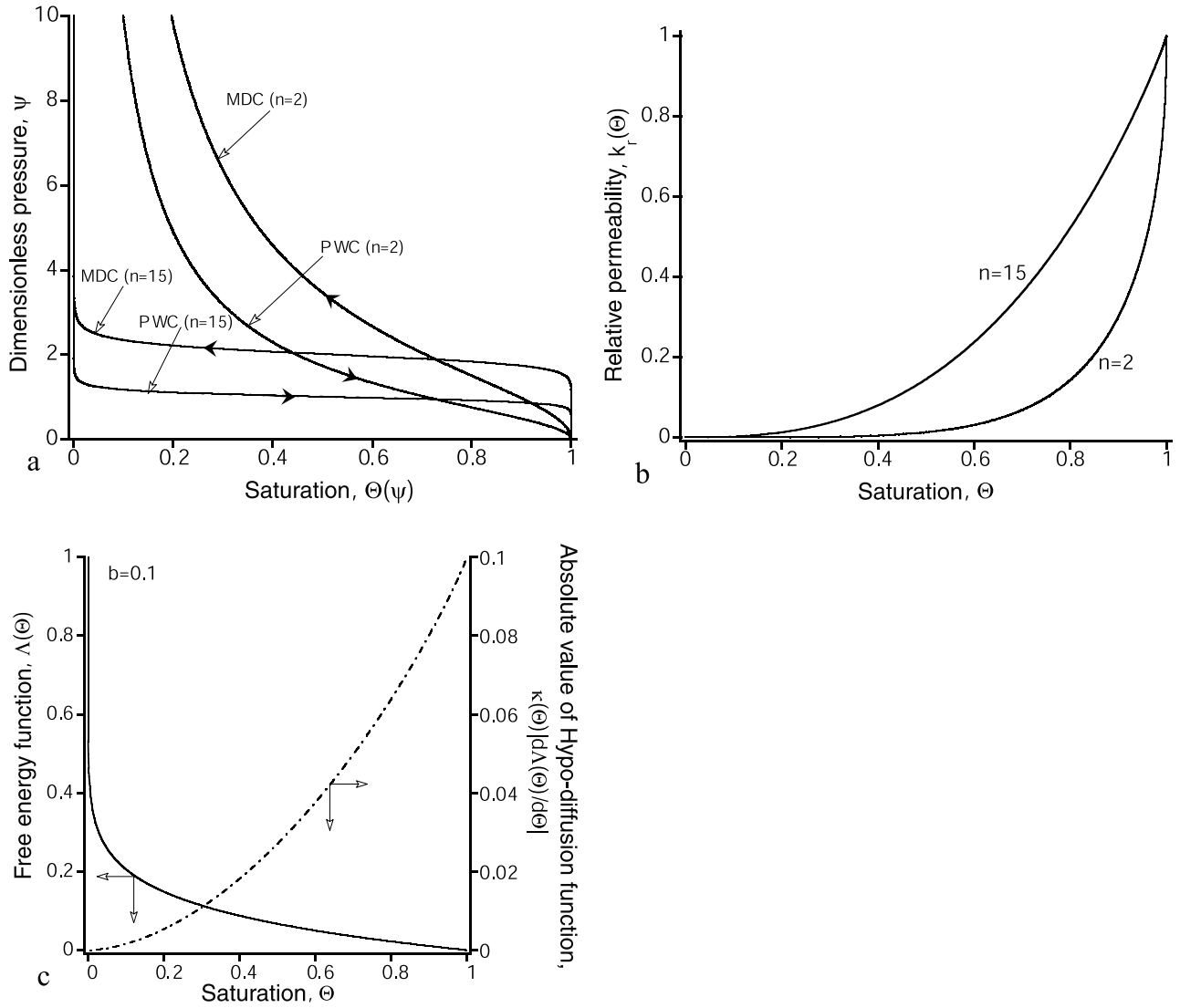


Figure 1. Standard monotonic properties as typically measured for unsaturated porous materials as well as an assumed form of the free energy function. (a) Hysteretic pressure-saturation (i.e., equation of state) relations for the primary wetting curve (PWC) and main drainage curve (MDC) for $n = 2$ that does not normally display gravity-driven fingers (GDF) are compared to $n = 15$ curves, where GDF is typically observed to occur. The pressure-saturation curves are developed using (12a) for dimensionless $\alpha^* = 1$ for the PWC and $\alpha^* = 0.5$ for the MDC. Here we assume both the PWC and the MDC are scaled to have the same maximum saturation value of 1 (i.e., we are not considering the effects of air and water entrapment on the PWC and the MDC, respectively). (b) Relative permeability as a function of saturation (i.e., constitutive relation), which normally does not display a hysteretic response, is evaluated using (12b) for $n = 2$ and $n = 15$ materials. (c) Functional response of the dimensionless free energy, $\Lambda(\Theta)$, evaluated using (12c) for $b = 0.1$, is compared with the absolute value of the hypodiffusion function, $\kappa(\Theta)|\partial\Lambda/\partial\Theta|$.

evaluate $\Theta(\psi)$ for the PWC and MDC, respectively, and (12b) is used to arrive at the nonhysteretic relative permeability function, $\kappa(\Theta)$ function. The functional form of $\Lambda(\Theta)$, using (12c) with $b = 0.1$, and its comparison with $\kappa(\Theta)|\partial\Lambda/\partial\Theta|$ is displayed in Figure 1c. Although at low or near zero saturations, $\partial\Lambda/\partial\Theta$ yields large negative values (i.e., in the limit, as $\Theta \rightarrow 0$, $\partial\Lambda/\partial\Theta \rightarrow -\infty$), the functional form of $\kappa(\Theta)|\partial\Lambda/\partial\Theta|$ is controlled in this region by the relative permeability function, $\kappa(\Theta)$. However, as full saturation is approached, $\partial\Lambda/\partial\Theta \rightarrow -b$ and thus $\kappa(\Theta)|\partial\Lambda/\partial\Theta| \rightarrow b$.

[12] Finally, to predict the higher-order scanning hysteretic branches, we employ Scott's model of hysteresis [Scott

et al., 1983]. Scott's model is an empirical approach that predicts the higher-order scanning (wetting or drying) curves by simply scaling the bounding curves (i.e., PWC and MDC within the context of present work). For instance, the pressure-saturation function for a scanning drainage curve (SDC) can be stated as:

$$\Theta_{SDC}(\Psi) = \Theta_{sd}\Theta_{MDC}(\Psi) \quad (13a)$$

$$\Theta_{sd} = \frac{\Theta_{RW}}{\Theta_{MDC}(\Psi_{RW})} \quad (13b)$$

where $\Theta_{SDC}(\Psi)$ is the SDC as a function of pressure, Ψ , Θ_{sd} is the corresponding saturated (or satiated) value for the SDC, $\Theta_{MDC}(\Psi)$ describes the functional form of MDC obtained from (12a) with $\alpha^* = 0.5$, and Θ_{RW} and Ψ_{RW} , respectively, are the reversal saturation and pressure on the wetting branch issuing the new SDC. Similarly, to find the functional form of a scanning wetting curve (SWC):

$$\Theta_{SWC}(\Psi) = \Theta_{rw} + (1 - \Theta_{rw})\Theta_{BWC}(\Psi) \quad (14a)$$

$$\Theta_{rw} = \frac{\Theta_{RD} - \Theta_{BWC}(\Psi_{RD})}{1 - \Theta_{BWC}(\Psi_{RD})} \quad (14b)$$

where $\Theta_{SWC}(\Psi)$ is SWC as a function of Ψ , Θ_{rw} is the corresponding residual saturation value for the new SWC, $\Theta_{BWC}(\Psi)$ describes the boundary wetting curve (BWC) that here we consider to be PWC evaluated using (12a) with $\alpha^* = 1$, and Θ_{RD} and Ψ_{RD} refer to the reversal saturation and pressure values on the drying branch where SWC is issued from, respectively. We note that (13) and (14) are stated for closed-loop hysteresis curves, i.e., the bounding curves have the same residual and saturated (or satiated) moisture contents, which within our dimensionless forms are zero and one, respectively.

2.2. One-Dimensional Form of Initial Boundary Value Problem

[13] In this paper, the majority of our analysis is focused on the one-dimensional (1D) HDE (sections 3 and 4). The 1D Initial Boundary Value Problem (IBVP) is defined as follows. From (10), we write the dimensionless 1D representation of the HDE as:

$$\left(\frac{\partial\Theta(\Psi)}{\partial\Psi}\right)\frac{\partial\Psi}{\partial\tau} = \frac{\partial}{\partial\xi}\left[\kappa(\Theta)\frac{\partial\Psi}{\partial\xi}\right] + \delta\frac{\partial\kappa(\Theta)}{\partial\xi} + N_{HD}\frac{\partial}{\partial\xi}\left[\left(\kappa(\Theta)\frac{\partial\Lambda}{\partial\Theta}\right)\frac{\partial\Theta(\Psi)}{\partial\xi}\right] \quad (15)$$

Assuming a uniform initial saturation of Θ_i in the entire domain, we define the initial condition as:

$$\Theta(\xi, 0) = \Theta_i \quad \text{for} \quad -Z^* \leq \xi \leq 0 \quad (16)$$

where $Z^* = \alpha_{PWC}Z$ is the dimensionless domain size in the vertical direction and Z [L] signifies the domain's physical height. We also state the boundary conditions most generally as:

$$\beta_0\left\{-\kappa\left[\left(\frac{\partial\Psi}{\partial\xi} + \delta\right) + N_{HD}\left(\frac{\partial\Lambda}{\partial\Theta}\right)\frac{\partial\Theta}{\partial\xi}\right]\right\}_{B_i} + \beta_1\Psi|_{B_i} = F_i \quad (17)$$

along the boundary B_i , where β_0 and β_1 are constants that depending on the boundary condition type, can take on values of either zero or one, B_i denotes the boundary (e.g., top or bottom in the vertical sense or left and right in the horizontal sense), and F_i represents the boundary condition value [e.g., see *Ozisik*, 1980 p. 14]. In general, (17) allows a greater flexibility to explore the HDE numerical solution for both constant flux and prescribed pressure boundary conditions. For instance, letting B_i

represent the top (surface) boundary, for $\beta_0 = 1$, $\beta_1 = 0$, $F_i = R_s$, we have constant flux boundary conditions. Similarly, for $\beta_0 = 0$, $\beta_1 = 1$, and $F_i = \psi_{in}$, (17) becomes a constant head or prescribed boundary condition. Here $R_s = q_s/K_s$ is the dimensionless surface flux ratio and $\psi_{in} = \alpha_{PWC}\Psi_{in}$ is a dimensionless prescribed pressure, with q_s [LT^{-1}] and Ψ_{in} [L] being the surface flux and prescribed pressure values, respectively. Similar conditions can also be stated for the bottom boundary and/or when considering horizontal imbibition case (i.e., $\delta = 0$). For solutions of the 2D IBVP (section 5.1), the 1D IBVP is straightforwardly extended with uniform top and bottom boundary conditions.

3. One-Dimensional Numerical Discretization and Solution Approach

[14] To discretize and solve the 1D IBVP, (15) to (17), we employ a fully implicit cell-centered finite difference approach, similar to that discussed by *Eliassi and Glass* [2001a]. Using a first-order backward Euler to evaluate the temporal derivative and only considering constant grid spacing, we can write the discretized form of (15) as:

$$\frac{1}{\Delta\tau_{\nu+1}}\left(\frac{\partial\Theta}{\partial\Psi}\right)_j^{\nu+1}\Psi_j^{\nu+1} - \frac{1}{\Delta\xi^2}\left[\kappa_{j+1/2}^{\nu+1}(\Psi_{j+1}^{\nu+1} - \Psi_j^{\nu+1}) - \kappa_{j-1/2}^{\nu+1}(\Psi_j^{\nu+1} - \Psi_{j-1}^{\nu+1})\right] = r_j^{\nu+1} \quad (18a)$$

where $\Delta\tau_{\nu+1}$ is the current time step size, subscript j refers to the nodal points in ξ direction, superscript $\nu + 1$ is the index for the current time step, $\Delta\xi$ is the dimensionless uniform grid spacing, and $\kappa_{j\pm 1/2}^{\nu+1}$ are the average κ values across two connected nodes. $r_j^{\nu+1}$ has the following form:

$$r_j^{\nu+1} = \frac{1}{\Delta\tau_{\nu+1}}\left(\frac{\partial\Theta}{\partial\Psi}\right)_j^{\nu+1}\Psi_j^{\nu} + \frac{\delta}{\Delta\xi}\left[\kappa_{j+1/2}^{\nu+1} - \kappa_{j-1/2}^{\nu+1}\right] + N_{HD}\frac{1}{\Delta\xi^2}\left[\left(\kappa\frac{\partial\Lambda}{\partial\Theta}\right)_{j+1/2}^{\nu+1}(\Theta_{j+1}^{\nu+1} - \Theta_j^{\nu+1}) - \left(\kappa\frac{\partial\Lambda}{\partial\Theta}\right)_{j-1/2}^{\nu+1}(\Theta_j^{\nu+1} - \Theta_{j-1}^{\nu+1})\right] + \left[\beta_0\frac{R_s}{\Delta\xi} + \beta_1\Psi_{in}\right]_{B_i} \quad (18b)$$

where superscript ν is the previous time step index and the last group of terms on the RHS of (18b) refers to the boundary conditions. When considering flux boundary conditions (i.e., $\beta_0 = 1$ and $\beta_1 = 0$), the index j extends over, $0 \leq j \leq J + 1$ ($j = 0$ and $j = J + 1$ refer to the mesh indices for the two boundaries). However, when we have a prescribed top boundary condition (e.g., at $j = 0$), in (18b) $\beta_0 = 0$ and $\beta_1 = 1$ and $1 \leq j \leq J + 1$. A similar procedure is used if a prescribed pressure is at $j = J + 1$, e.g., capillary rise in a vertical domain and/or considering horizontal imbibition, where $\delta = 0$.

[15] At the start of each time step, we calculate the time step size, $\Delta\tau_{\nu+1}$, using:

$$\Delta\tau_{\nu+1} = \min(\lambda\Delta\tau_{\nu+1}, \Delta\tau_{CFL}, \Delta\tau_{HD}, \Delta\tau_{max}) \quad (19a)$$

where $\lambda = 1.1$ is a time step growth factor, $\Delta\tau_\nu$, $\Delta\tau_{CFL}$, $\Delta\tau_{HD}$, and $\Delta\tau_{max}$ refer to the previous, advective, hypodiffusive, and maximum time step sizes, respectively, with $\Delta\tau_{max} = 10^{-3}$. We also define $\Delta\tau_{CFL}$ and $\Delta\tau_{HD}$, respectively as:

$$\Delta\tau_{CFL} = \nu_{CFL} \frac{\Delta\xi}{|v_{max}|} \quad (19b)$$

$$\Delta\tau_{HD} = \nu_{HD} \frac{\Delta\xi^2}{N_{HD}(\kappa|\partial\Lambda/\partial\Theta|)_{max}} \quad (19c)$$

where $\nu_{CFL} = 0.1$ and $\nu_{HD} = 0.5$ are the safety factors that limit the sizes of $\Delta\tau_{CFL}$ and $\Delta\tau_{HD}$, respectively, v_{max} is the maximum dimensionless velocity (i.e., ratio of flux to saturation), and the denominator in (19c) refers to the maximum (positive) value of the hypodiffusion function.

[16] To evaluate the internodal averages, i.e., the coefficients that include subscripts, $j \pm 1/2$, we considered the first-order upwind (UW1) and the second-order centered difference (CD2) averaging methods. In general diffusive applications, UW1 does not generate spurious oscillations and always yields physically relevant solutions [e.g., see *Forsyth and Kropinski, 1997*], even though its leading truncation error (LTE) causes an artificial diffusion of the WF. For small enough $\Delta\xi$ values, CD2 generally results in a smaller LTE and resolves sharp fronts better without the artificial diffusion found in UW1 or oscillations generated by higher-order methods [e.g., *Eliassi and Glass, 2001a*]. The formulation for both the UW1 and CD2 averaging methods can be generally stated as [*Eliassi and Glass, 2001a*]:

$$\gamma_{j+1/2}^{\nu+1} = \frac{1}{2} \left[(1 + w s_{j+1/2}) \gamma_j^{\nu+1} + (1 - w s_{j+1/2}) \gamma_{j+1}^{\nu+1} \right] \quad (20a)$$

where γ refers to the variable to be averaged, w is a weighting parameter, and $s_{j+1/2}$ determines the sign of the difference in γ between two adjacent nodes as:

$$s_{j+1/2} = \text{sgn}(\gamma_j^{\nu+1} - \gamma_{j+1}^{\nu+1}) = \begin{cases} 1 & \text{if } (\gamma_j^{\nu+1} - \gamma_{j+1}^{\nu+1}) \geq 0 \\ -1 & \text{if } (\gamma_j^{\nu+1} - \gamma_{j+1}^{\nu+1}) < 0 \end{cases} \quad (20b)$$

When considering the CD2 method, $w = 0$, and we only need to use (20a). However, for the UW1 method, we let $w = 1$.

[17] To linearize the system of nonlinear algebraic equations, resulting from (18a) and (18b), we first considered the modified Picard iteration (MPI) approach [e.g., *Celia et al., 1990*]. However, in a number of preliminary solutions of the HDE, we found the MPI method often would result in convergence problems and severe time step reduction [see *Eliassi, 2001*]. For this reason, we chose the one-step noniterative linearization (OSNL) approach [e.g., *Haverkamp et al., 1977*], which yielded a global mass balance error on the order of 0.1% or smaller for all solutions reported in this paper. In the OSNL approach, we simply evaluate the various nonlinear variables using the information from the previous time cycle, ν . We can then write the

following compact form, for the system of linear equations to be solved at each time step:

$$[D(\Psi^\nu)]\{\Psi^{\nu+1}\} = \{r(\Psi^\nu)\} \quad (21)$$

where $[D(\Psi^\nu)]$ is the linear coefficients matrix, which is evaluated using the known vector $\{\Psi^\nu\}$, $\{\Psi^{\nu+1}\}$ represents the unknown pressure vector, and $\{r(\Psi^\nu)\}$ is the RHS vector in (18b) which is also evaluated using $\{\Psi^\nu\}$ values. To arrive at the unknown pressure values, $\{\Psi^{\nu+1}\}$, at each time step for 1D cases, we use the Thomas algorithm to directly solve the system of linear equation [e.g., *Anderson et al., 1984*, p. 128].

[18] Following matrix inversion, we assess the hysteretic state of each node by checking the changes in the nodal pressures from the previous time step (i.e., $\Delta\Psi_j^{\nu+1} = \Psi_j^{\nu+1} - \Psi_j^\nu$). If at node, j , the sign of $\Delta\Psi_j^{\nu+1}$ has changed and $|\Delta\Psi_j^{\nu+1}| > \varepsilon_H$, that node is placed on a new hysteretic branch and (13) or (14) are used to update the hysteretic equation of state, $\Theta(\Psi)$. Here ε_H is the dimensionless reversal threshold and is set to a small number, where $\varepsilon_H = 10^{-8}$. We choose a small ε_H value, as it allows for all reversals to naturally occur and the reversal criterion is not tied to any other property of the $\Theta(\Psi)$ (e.g., α or the inverse capillary rise). Once $\Theta(\Psi)$ has been updated, we also update $\partial\Theta(\Psi)/\partial\Psi$, $\kappa(\Theta)$, and $\Lambda(\Theta)$ for the current time and advance to the next time cycle.

3.1. Sensitivity to Grid Resolution and Averaging Methods

[19] To illustrate the basic response of the HDE numerical solution as well as its sensitivity to the grid spacing, $\Delta\xi$, we first present the solution where $N_{HD} = 5$. We consider a vertically oriented domain (i.e., $\delta = 1$) with $Z^* = -20$, under an initially dry condition ($\Theta_i = 10^{-10}$), and highly nonlinear porous medium ($n_{PWC} = 15$), where the top boundary is subject to a constant flux of $R_s = 0.1$, and the bottom boundary has a zero flux condition. Other related physical and numerical parameters are listed in Table 1 under the baseline case. Figure 2 depicts the saturation and pressure profiles using the CD2 (Figures 2a and 2b) and UW1 (Figures 2c and 2d) averaging methods for grid spacings of $\Delta\xi = 0.08, 0.04, 0.02$, and 0.01 . For both averaging methods the solution is nonmonotonic with both the saturation and pressure rising as the WF is approached and then dropping further behind where they eventually take on an asymptotic value. While for all $\Delta\xi$ values the CD2 (Figure 2a) method yields a fully saturated finger tip, for the UW1 (Figure 2c) the finger becomes fully saturated only as the $\Delta\xi$ decreases. We note that contrary to what we have found for the RE where nonmonotonic solutions caused by numerical artifacts become monotonic as the grid is refined [*Eliassi and Glass, 2001a*], the nonmonotonicity in the HDE solution enhances as the grid is refined.

3.2. Evaluation of Truncation Errors

[20] To understand the response of the HDE solution as a function of grid spacing and averaging method, we can consider the LTE of each averaging method, and evaluate the corresponding ‘‘modified governing equation’’ (MGE) for the HDE. *Eliassi and Glass* [2001a] derived the MGE for the RE numerical solution (i.e., the equation that is actually being solved during the numerical solution steps).

Table 1. Dimensionless Physical and Numerical Parameters for 1D Solutions

Parameter	Value
Parameters for baseline case ^a	
Material nonlinearity for PWC, n_{PWC}	15
Material nonlinearity for MDC, n_{MDC}	15
Inverse capillary pressure, $\alpha_H^* = \alpha_{MDC}^*/\alpha_{PWC}^*$	0.5 (hysteretic)
Hysteretic reversal criterion, ε_H	10^{-8}
Domain height, Z^*	20
Initial saturation, Θ_i	10^{-10}
Applied flux ratio, R_s	0.1
Flow direction, δ	1 (vertical)
Free energy function exponent, b	0.1
Hypodiffusion number, N_{HD}	2
Maximum solution time, τ_{max}	60
Spatial grid spacing, $\Delta\xi$	0.01
Averaging method	CD2
Linearization scheme	OSNL
Parameters for section 3.1 (Figure 2): Effects of grid resolution and averaging methods	
Spatial grid spacing, $\Delta\xi$	0.08, 0.04, 0.02, 0.01
Averaging method	CD2, UW1
Hypodiffusion number, N_{HD}	5
Parameters for section 4.1 (Figure 4): Effect of hypodiffusion number	
Hypodiffusion number, N_{HD}	0, 0.2, 1, 2, 5, 10, 15, 20
Parameters for section 4.2 (Figure 7): Effect of initial saturation	
Initial saturation, Θ_i	$10^{-10}, 10^{-5}, 10^{-4}, 10^{-3}, 10^{-2}$
Parameters for section 4.3 (Figure 8): Effect of applied flux ratio	
Initial saturation, R_s	$10^{-4}, 10^{-3}, 0.01, 0.1, 0.4, 0.5, 0.75, 0.9, 1$
Corresponding τ_{max}	6000, 2250, 400, 60, 15, 12, 8, 6.5, 6
Parameters for section 4.4 (Figure 9): Effect of media nonlinearity	
Material nonlinearity for PWC, n_{PWC}	2, 3, 5, 9, 11, 15 (note we let $n_{MDC} = n_{PWC}$)
Parameters for section 4.5: Effects of horizontal imbibition and capillary rise	
Horizontal imbibition (Figure 10)	
Flow direction, δ	0
Applied flux ratio, R_s	0.1
Prescribed pressure boundary condition (BC), Ψ_{in}	-0.25
Capillary rise (Figure 11)	
Surface (top) BC, R_s	0
Bottom BC, Ψ_{in}	0

^aUnless otherwise stated, all parameters for subsequent sections are the same as the baseline case.

Using a similar approach, we can write the MGE for the 1D form of the HDE as:

$$\begin{aligned} & \left(\frac{\partial \Theta}{\partial \Psi} \right) \frac{\partial \Psi}{\partial \tau} - \frac{\partial}{\partial \xi} \left[\kappa \left(\frac{\partial \Psi}{\partial \xi} \right) \right] - \delta \frac{\partial \kappa}{\partial \xi} - N_{HD} \frac{\partial}{\partial \xi} \left[\left(\kappa \frac{\partial \Lambda}{\partial \Theta} \right) \frac{\partial \Theta}{\partial \xi} \right] \\ & = -(E_T + E_C + E_G + E_{HD}) \end{aligned} \quad (22)$$

where the left-hand side is the 1D form of the HDE stated in (15) and the RHS refers to the LTE for the temporal, E_T , capillary, E_C , gravity, E_G , and hypodiffusive, E_{HD} , terms. Here we simply neglect E_T , since we have found the temporal term's LTE, in general, to be much smaller than the LTE for the spatial terms [see also *Eliassi and Glass, 2001a*]. For the CD2 averaging method, the LTE for the three spatial terms can be stated as:

$$\begin{aligned} E_C + E_G + E_{HD} &= \left(\frac{\Delta \xi^2}{6} \right) \left[\frac{1}{2} \frac{\partial^2}{\partial \xi^2} \left(\kappa \frac{\partial^2 \Psi}{\partial \xi^2} \right) \right. \\ & \quad \left. + \frac{\partial}{\partial \xi} \left(\frac{\partial^2 \kappa \partial \Psi}{\partial \xi^2 \partial \xi} \right) \right] + \left(\frac{\Delta \xi^2}{6} \right) \frac{\partial^3 \kappa}{\partial \xi^3} \\ & \quad + N_{HD} \left(\frac{\Delta \xi^2}{6} \right) \left[\frac{1}{2} \frac{\partial^2}{\partial \xi^2} \left(\left(\kappa \frac{\partial \Lambda}{\partial \Theta} \right) \frac{\partial^2 \Theta}{\partial \xi^2} \right) \right. \\ & \quad \left. + \frac{\partial}{\partial \xi} \left(\frac{\partial^2}{\partial \xi^2} \left(\kappa \frac{\partial \Lambda}{\partial \Theta} \right) \frac{\partial \Theta}{\partial \xi} \right) \right] \end{aligned} \quad (23a)$$

and for the UW1 averaging method, they become:

$$\begin{aligned} E_C + E_G + E_{HD} &= \left(\frac{\Delta \xi}{2} \right) \frac{\partial}{\partial \xi} \left(\frac{\partial \kappa \partial \Psi}{\partial \xi \partial \xi} \right) + \left(\frac{\Delta \xi}{2} \right) \frac{\partial^2 \kappa}{\partial \xi^2} \\ & \quad + N_{HD} \left(\frac{\Delta \xi}{2} \right) \frac{\partial}{\partial \xi} \left(\frac{\partial}{\partial \xi} \left(\kappa \frac{\partial \Lambda}{\partial \Theta} \right) \frac{\partial \Theta}{\partial \xi} \right) \end{aligned} \quad (23b)$$

In (23a) and (23b), the first, second, and third terms correspond to E_C , E_G , and E_{HD} LTE, respectively.

[21] Figure 3 compares the variation in the total spatial LTE (i.e., the RHS of (22) disregarding E_T) with that of the hypodiffusive term, for the smallest grid spacing considered (i.e., $\Delta \xi = 0.01$). Here we focus our examination near the WF where the pressure and saturation gradients are greatest. To evaluate the various terms (i.e., the LTE and/or the hypodiffusive term), we use the computed results at the given time along with the same finite difference approach used to discretize the various terms within the HDE. We see that the hypodiffusive term has the required negative minimum (i.e., hold-back) and positive maximum (i.e., pile-up) as the WF is crossed. We also find the total spatial LTE generally to have a similar behavior as the hypodiffusive term; thus it slightly enhances the HBPU effect. However, for $\Delta \xi = 0.01$ the LTE magnitudes are much less than the size of the hypodiffusive term and thus do not dominate the numerical solution and/or the response of the HDE. Additionally, relative to the hypodiffusive term, we note that the

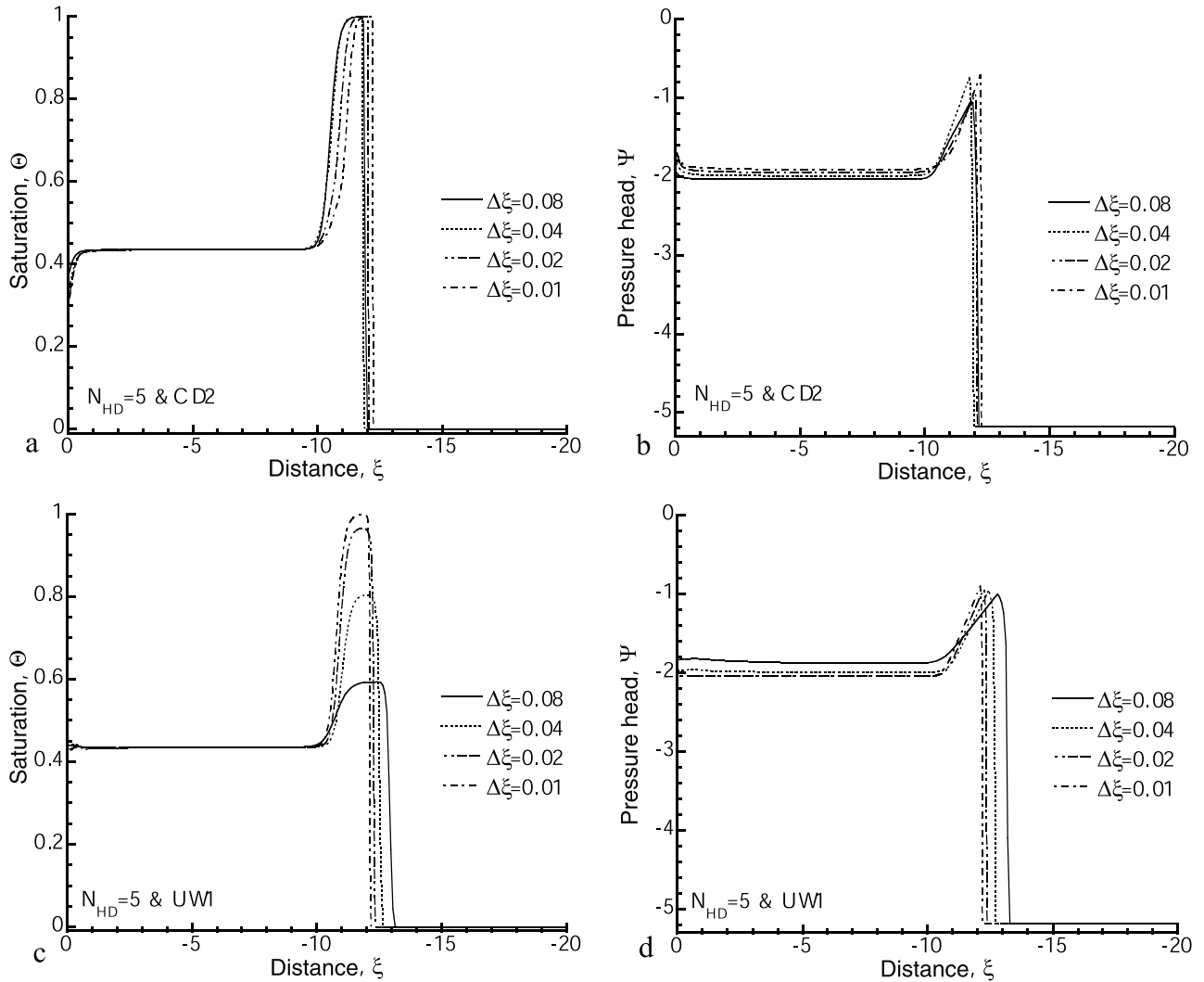


Figure 2. Saturation and pressure profiles, obtained using numerical solution of the hypodiffusive governing equation, illustrate the influences of grid spacing, $\Delta\xi$, and averaging method for a hypodiffusion number of $N_{HD} = 5$. For the CD2 averaging method: (a) saturation profiles are nearly identical as $\Delta\xi$ reduces but with slight variations in the WF position for different $\Delta\xi$ values; (b) pressure profiles show slight variations in the peak pressure at the WF. For the UW1 averaging method: (c) finger tip saturation increases as $\Delta\xi$ reduces; (d) pressure profiles show the WF sharpens as smaller $\Delta\xi$ are used, with little variation in the peak pressure among the various profiles.

LTE for the CD2 (Figure 3a) solution is noticeably smaller than that of UW1 (Figure 3b).

[22] While (23a) and (23b) show the LTE to decrease with grid refinement, because the hypodiffusive term itself is a “self-sharpener,” it is possible that such refinement could cause the hypodiffusive term to overwhelm the solution and cause pressures to become unbounded. To consider this possible effect, we conducted a simulation for $N_{HD} = 2$ where the grid spacing was further reduced by an order of magnitude (i.e., $\Delta\xi = 0.001$). Solutions yielded peak pressure values at the WF that were quite comparable (e.g., -0.94 for $\Delta\xi = 0.01$ versus -0.96 for $\Delta\xi = 0.001$). While not an exhaustive proof, this “taming” of the hypodiffusive term must occur through feedback within the HDE from the stabilizing capillary term, and thus, as we continue to refine the grid, pressure appears to remain bounded. Of course, increasing N_{HD} itself beyond a thresh-

old value (~ 30 for CD2) can indeed result in unbounded pressures.

4. One-Dimensional Numerical Illustrations Using HDE

[23] Here we first examine the 1D numerical response of the HDE with respect to N_{HD} . Then for a single value of N_{HD} , we consider solution behavior as a function of the critical physical parameters that control GDF which, as discussed by *Glass and Nicholl* [1996], include the initial moisture content, Θ_i , the flux ratio, R_s , the media nonlinearity, n_{PWC} , and of course flow direction, δ (i.e., vertical downward, vertical upward, and horizontal). The various physical and numerical parameters for all the illustrations are summarized in Table 1. A full set of solutions was conducted for both the UW1 and CD2 methods. However,

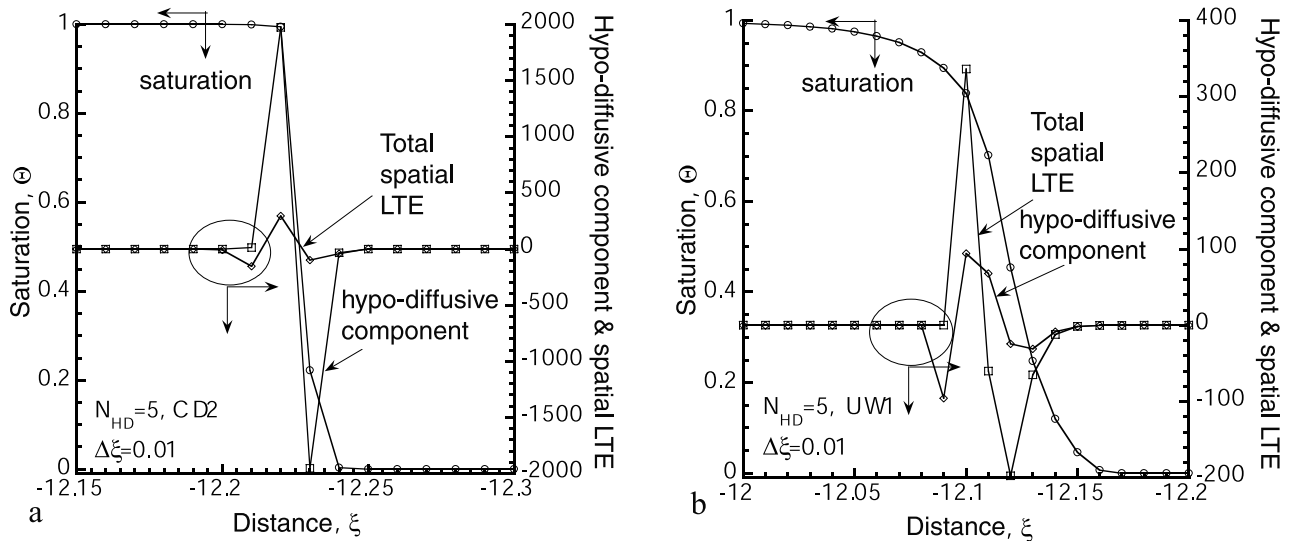


Figure 3. Functional behaviors of the hypodiffusive term and the total spatial leading truncation error (right-hand vertical axis) are shown near the wetting front along with the saturation profile (left-hand vertical axis) for the solutions with $\Delta\xi = 0.01$ presented in Figure 2: (a) for the CD2 averaging method and (b) for the UW1 averaging method.

for the sake of brevity, and because of the reduced truncation error demonstrated for the CD2 averaging method, as well as the fact that CD2 resolves the WF more sharply than UW1, we present results primarily for CD2 below.

4.1. Effect of Hypodiffusion Number on the HDE Solution

[24] As shown in Figure 4, over the range of N_{HD} values listed in Table 1, the saturation and pressure profiles transition from monotonic for $N_{HD} \leq 1$, where they all are nearly identical to that of the standard RE (i.e., when $N_{HD} = 0$), to nonmonotonic for $N_{HD} \geq 2$. The solution for

the $N_{HD} = 2$ is quite similar to the $N_{HD} = 5$ (previously shown in Figure 2c). That is, the 1D “finger tip” is fully saturated and drains behind to an asymptotic value. The peak pressure for $N_{HD} = 2$ is barely greater than the monotonic solution (i.e., $N_{HD} \leq 1$) (see Figure 4b). This small difference in pressure is due to the extra “kick” that the hypodiffusion term provides at the WF to create non-monotonic profiles. For $N_{HD} \geq 10$, while the finger tip is also fully saturated, the profile overdrains behind the WF and then approaches an asymptotic saturation from below. Additionally, the WF positions for $N_{HD} = 15$ and 20 do not advance as far into the domain and have longer saturated

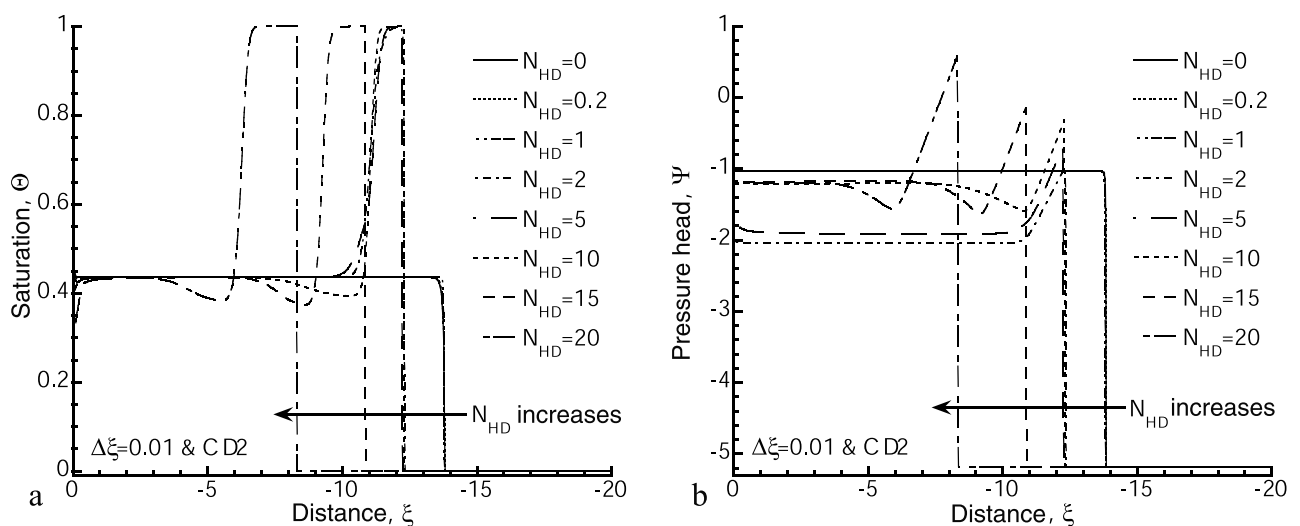


Figure 4. Effect of hypodiffusion number, N_{HD} , on the numerical solution of HDE for the $\Delta\xi = 0.01$ case in Figure 2a: (a) saturation profiles show there is a transition from monotonic to nonmonotonic responses as N_{HD} increases, but larger N_{HD} values oversharpen and slow down the wetting front advancement, and (b) pressure profiles show the peak pressure increases as a function of N_{HD} and when $N_{HD} = 20$ the solution yields positive pressures, which is unphysical for water wettable materials.

finger tips than those for $N_{HD} \leq 10$. Considering the pressure profiles (Figure 4b), for $N_{HD} \geq 1$ the peak pressure value (i.e., the pressure at the WF) continually increases, until for $N_{HD} = 20$, the peak pressure is positive. For water wettable porous materials, pressures should always remain in tension, and thus large N_{HD} values may not be physically relevant to our problem.

[25] To better understand the behavior of the HDE, we evaluate the response of the gravity, capillary, and hypodiffusive terms as we cross the WF. In Figure 5 we plot each term along with the saturation profile for $N_{HD} = 2$. The magnitudes of the capillary and hypodiffusive terms are both seen to be much greater than that of the gravity term. Additionally, the capillary term's profile is the mirror image of the hypodiffusive (i.e., there is a positive maximum ahead of the WF and a negative minimum behind the WF) and of nearly equal but opposite magnitude. Thus the capillary and hypodiffusive terms are in direct and nearly equal competition. Analyzing the profiles in Figure 4, we find for $N_{HD} > 2$, the capillary and hypodiffusive term magnitudes increase with N_{HD} , but at the front edge of the WF (first swing on Figure 5 where the maximum absolute value of each term is found) the capillary term always slightly out competes the hypodiffusive for the range of N_{HD} considered (Figure 6). For $N_{HD} \leq 2$, the relative importance of the hypodiffusive term decreases, eventually yielding a monotonic solution. On the basis of this behavior we choose a value of $N_{HD} = 2$ in subsequent simulations to consider the critical physical parameters that control GDF (sections 4.2–4.5).

4.2. Effect of Initial Saturation

[26] Saturation profiles for the $N_{HD} = 2$ case using a range of initial saturation, $10^{-10} \leq \Theta_i \leq 0.01$ (Table 1), are shown

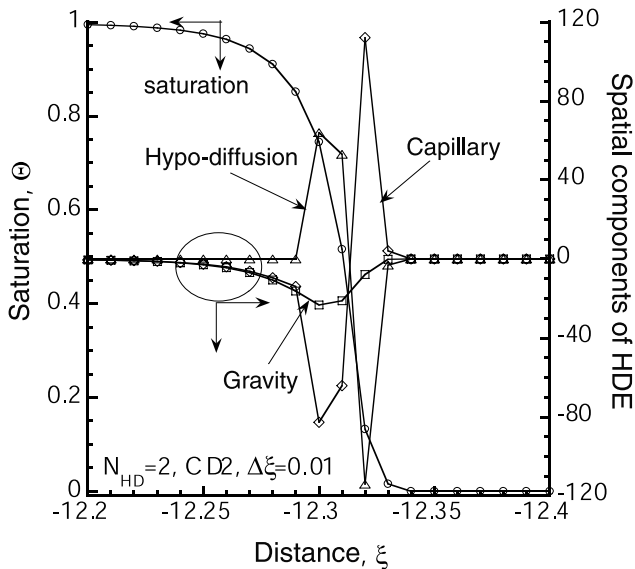


Figure 5. Local behaviors of the spatial terms in the hypodiffusive governing equation (left-hand vertical axis) are plotted along with the saturation profiles (right-hand vertical axis) near the wetting front for the baseline case (i.e., $N_{HD} = 2$) shown in Figure 4. The capillary and the hypodiffusive terms have nearly equal but opposite behaviors. Note that compared to the two other spatial terms, the gravity term is of much smaller magnitude.

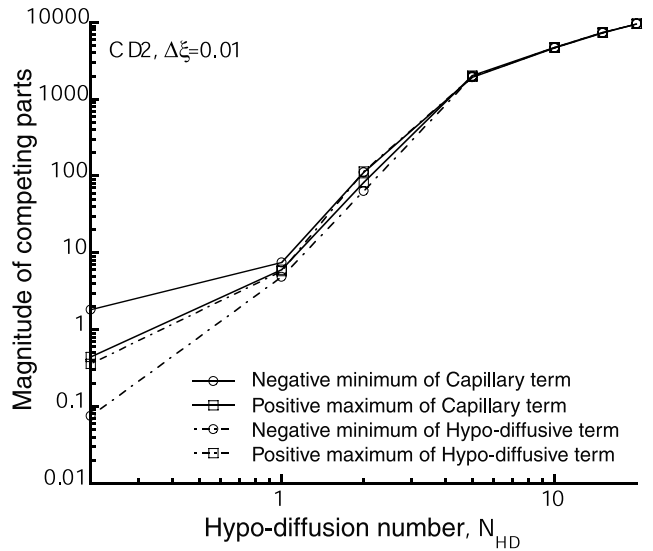


Figure 6. Positive maximum and the absolute value of the negative minimum of the competing parts of the capillary and hypodiffusive terms versus N_{HD} for the solutions in Figure 4. As N_{HD} increases, the magnitude of each term also grows; however, the hypodiffusive term is never larger than the capillary term for the range of N_{HD} values shown.

in Figure 7. Over the range $10^{-10} \leq \Theta_i \leq 10^{-4}$ the solutions are nearly identical and for $\Theta_i \leq 10^{-3}$, while the finger tip saturation is the same as the cases with lower Θ_i , by mass balance the profile moves slightly further into the domain. As the initial saturation increases to $\Theta_i = 0.01$, the profiles become monotonic. This trend toward monotonicity with increasing initial saturation is consistent with previous experimental observations of GDF. For instance, *Diment and Watson* [1985] found that as the uniformly distributed initial saturation increases, GDF becomes less distinct. Additionally, *Glass and Nicholl* [1996] demonstrated that

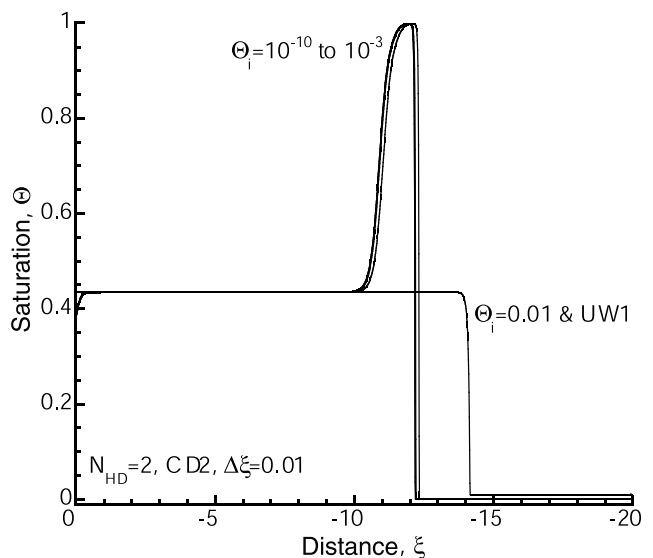


Figure 7. Saturation profiles for $N_{HD} = 2$ illustrating the effect of initial saturation, Θ_i , on the numerical solution of the HDE. The various profiles show that as Θ_i increases, the solution becomes monotonic.

if sand where GDF occurs under dry conditions is pre-wetted to a uniformly drained “field capacity,” a diffuse bulb instead of GDF forms from a point source. Formation of diffuse wetting fronts in initially moist sands that support GDF when dry, have also been reported by other investigators [e.g., Liu *et al.*, 1994; Sililo and Tellam, 2000].

4.3. Effect of Applied Flux Ratio

[27] Figure 8 displays saturation profiles for $N_{HD} = 2$ as a function of applied flux ratio, R_s , for the range $10^{-4} \leq R_s \leq 1$ (Table 1). For $0.1 \leq R_s \leq 1$, the solution time for each profile is chosen such as to have roughly the same mass within the domain. However, for $R_s \leq 10^{-2}$, finger tips would have extended beyond our problem domain and so these solutions are given before they reach the bottom boundary (see Table 1 for corresponding solution times). We see that, as R_s approaches a value of 1, the saturated tip length increases and the profiles trend toward monotonicity. In particular, for $R_s = 1$ (not shown in figure) the entire zone behind the WF is fully saturated. At the low flow extreme, we also see a trend toward monotonicity where for $R_s = 10^{-4}$, the profile is nearly monotonic.

[28] Experimental studies of GDF by Glass *et al.* [1989], found a simple relation for finger tip length, L_s , as a function of the flux through the finger R_f , as:

$$L_s = \frac{\Psi_{we} - \Psi_{ae}}{1 - R_f} \quad (24)$$

where the numerator, $\Psi_{we} - \Psi_{ae}$, signifies the difference between the water and air-entry pressures of the sand. Taking R_f to be analogous to R_s , in the limit as R_f goes to 1, the saturated tip length becomes infinite and, as R_f approaches zero, L_s simply becomes the size of the hysteresis loop (i.e., within the context of our dimensionless variables, $L_s \rightarrow 1$ as R_f becomes small). This behavior is qualitatively consistent with our current solutions for R_s at 10^{-3} and above. For very low R_s , Yao and Hendrickx [1996] have found more recently that quartz and perlite sands produced stable wetting fronts at $R_s \sim 10^{-4}$. Once again, our solutions also show this trend although the profile for $R_s = 10^{-4}$ is still not quite monotonic.

4.4. Effect of Material Nonlinearity

[29] Material nonlinearity, n_{PWC} , is another critical parameter that controls the occurrence of GDF. Saturation profiles shown in Figure 9, for the range $2 \leq n_{PWC} \leq 15$ (see Table 1), using $N_{HD} = 2$, demonstrate a transition from monotonic to nonmonotonic response when n_{PWC} is above 9. When $n_{PWC} = 9$ the WF becomes quite sharp and for $n_{PWC} = 11$ the finger tip saturation is ~ 0.7 , while for the baseline case (i.e., $n_{PWC} = 15$) a fully saturated finger tip forms. The transition from monotonic to nonmonotonic response conforms to experimental observations where GDF forms in materials with large n_{PWC} (e.g., sands), while GDF has not been observed in materials with small n_{PWC} (e.g., soils).

4.5. Horizontal Imbibition and Capillary Rise

[30] Finally, to demonstrate that the HDE complies with traditional understanding of flow through unsaturated porous materials, we consider two situations where monotonicity must always occur and GDF will not. The first is

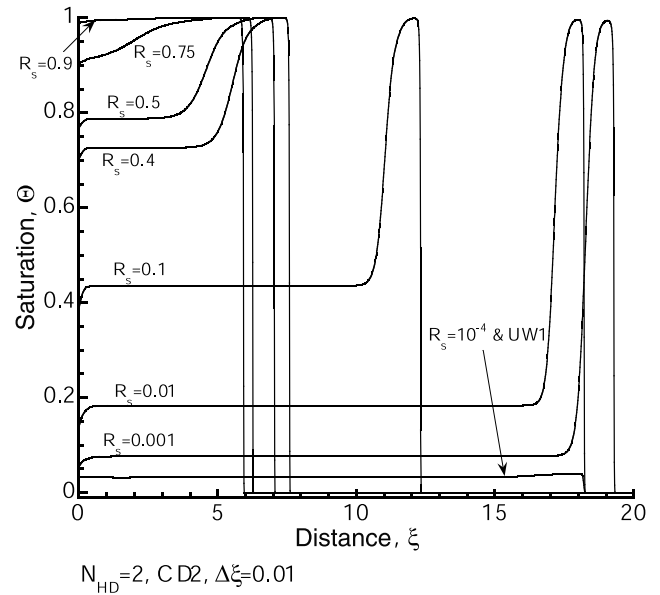


Figure 8. Saturation profiles for $N_{HD} = 2$ illustrating the effect of applied flux ratio, R_s , on the numerical solution of the HDE. While for $R_s = 0.9$, the solution is nearly monotonic and fully saturated, for the range $10^{-3} \leq R_s \leq 0.75$, the solution displays a nonmonotonic response, and finally for $R_s = 10^{-4}$, there is a transition back to monotonicity. With the exceptions of $R_s = 10^{-4}$, 10^{-3} , and 10^{-2} , the time for each profile is chosen so that there are roughly equal masses in the profile (see Table 1).

horizontal imbibition under both constant flux and constant pressure boundary conditions (where gravity is absent) and the second is capillary rise under a constant pressure boundary condition (where gravity acts to stabilize the flow). Figure 10 shows saturation profiles in the absence of the gravity, for the boundary conditions listed in Table 1. Comparing solutions for $N_{HD} = 0$ and $N_{HD} = 2$, under both R_s and Ψ_{in} type boundary conditions, we see that for both constant flux and prescribed pressure, the WF is fully saturated and all profiles are monotonic. However, the solutions for $N_{HD} = 2$ yield a much sharper WF than the $N_{HD} = 0$ cases. We also note that although all four profiles are at the same $\tau_{max} = 60$, the solutions for the Ψ_{in} boundary condition flow further into the domain as one would expect for unconstrained flux.

[31] To examine the HDE solution behavior for capillary rise, we use our baseline model and apply a prescribed pressure of $\Psi_{in} = 0$ at the bottom boundary and a zero flux condition to the top boundary (Table 1). Figure 11 shows the saturation profiles near the WF for $N_{HD} = 0$ and $N_{HD} = 2$ at the end of imbibition (i.e., at a time of $\tau_{max} = 30$). The saturation profile for the standard RE (i.e., $N_{HD} = 0$) approaches that of the equation of state (i.e., pressure-saturation curves), while for $N_{HD} = 2$, the profile is a bit sharper. We note that if one was to perform a capillary rise experiment and obtained a profile such as we have simulated with $N_{HD} = 2$, then use the equilibrium assumption based on the RE alone to derive the pressure-saturation relation for the medium, the n value would be significantly higher (e.g., $n \sim 45$). Obviously, a capillary rise simulation with RE using $n \sim 45$ will yield a profile that is near to that

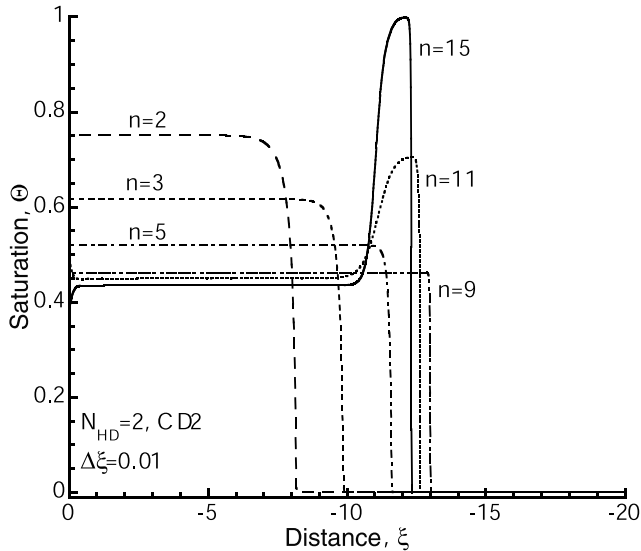


Figure 9. Saturation profiles for $N_{HD} = 2$ illustrating the effect of material nonlinearity, n_{PWC} , on the numerical solution of the HDE. While for $2 \leq n_{PWC} \leq 9$, the profiles are monotonic (with the $n_{PWC} = 9$ solution displaying a sharp wetting front), there is a transition to nonmonotonicity between n_{PWC} of 9 and 11.

obtained by the HDE with $N_{HD} = 2$. However, we note that solution of vertically downward flow (i.e., our baseline case) will be quite different with the RE (and $n \sim 45$) and HDE (and $n = 15$, $N_{HD} = 2$) yielding monotonic and nonmonotonic profiles, respectively.

5. Extensions

[32] The 1D analysis presented in sections 3 and 4 demonstrates that the HBPU effect, as modeled with the HD term, yields nonmonotonicity as a function of hypodiffusion number, N_{HD} , and also has the correct qualitative behavior with respect to physical parameters that limit GDF occurrence (i.e., initial dryness, applied flux ratio, material properties, and flow direction). Here we now demonstrate that this nonmonotonic behavior arising in the 1D solution indeed yields GDF in 2D (section 5.1). We then focus on the HBPU hypothesis presented by *Eliassi and Glass* [2002] and discuss nonmonotonicity and alternative forms of the HBPU effect (section 5.2). In particular, we show that the basic form of the HDE can be transformed to incorporate the HBPU effect into both modified constitutive relations and/or equations of state, both of which become nonmonotonic and thus can yield nonmonotonic solutions.

5.1. Two-Dimensional Simulations of GDF

[33] Our premise in the works of *Eliassi and Glass* [2001a, 2002] and throughout this paper has been that for a porous continuum approach to model GDF, nonmonotonicity must arise naturally from within the governing equation. Thus showing nonmonotonicity in the 1D solution implies that GDF will form in 2D. To illustrate this, we consider solutions of the 2D HDE. We simply extend our baseline 1D problem to be $H^* = 5$ units wide and implement zero flux boundary conditions to the left ($\eta = 0$), right ($\eta = H^*$), and bottom ($\xi = -Z^*$) boundaries, where η and

H^* , respectively denote the dimensionless horizontal direction and domain width. Similar to the baseline 1D cases, we choose the porous medium to be comprised of highly nonlinear material with $n_{PWC} = 15$, an initially uniform saturation of $\Theta_i = 10^{-10}$, and assume water is supplied across the entire top boundary (i.e., $\xi = 0$) at a constant and uniform flux of $R_s = 0.1$. Our 2D numerical solution approach is identical to that for 1D (section 3), except that we extend the finite difference discretization and CD2 averaging to the second dimension (i.e., η direction), and use an iterative solver to invert the resulting linear system of equations (for details, see *Eliassi and Glass* [2001a]).

[34] Figure 12 shows portions of the 2D solutions results for $N_{HD} = 0$ (i.e., the solution to the standard RE) and for $N_{HD} = 2$, along with an experimental saturation field from *Glass et al.* [1989]. Both experiment and numerical solutions are shown at the same scale in Figure 12 (see caption). Comparison of the two numerical solutions clearly shows that for the RE case (i.e., $N_{HD} = 0$) the WF is uniform and the solution is monotonic, while GDF forms for $N_{HD} = 2$. Additional solutions verify that the transition from monotonic to nonmonotonic in 1D is mirrored by monotonic to nonmonotonic GDF in 2D. Comparing the fields for the $N_{HD} = 2$ case and the experiment, we see many of the same qualitative features. Both show the field to rapidly break into fingers, fingers to merge, and a small number of strong fingers to dominate. We also see some differences such as the fact that the fingers in the experiment tend to meander more and have a more heterogeneous saturation structure. While the experimental flux was near to that in our numerical solution, it was not reported by *Glass et al.* [1989], and thus we cannot expect to match quantitative measures of finger velocities, widths, and saturated tip lengths exactly. Nevertheless, comparisons of the simulated and experimental results show that both average finger velocities and finger widths are within 20%, while saturated

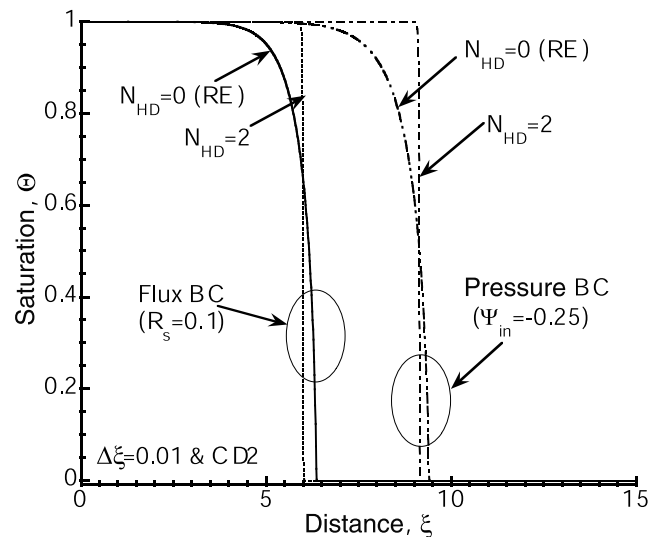


Figure 10. Saturation profiles for horizontal imbibition subject to either a constant flux ($R_s = 0.1$) or prescribed pressure ($\Psi_{in} = -0.25$). While for both types of boundary conditions the solution remains monotonic, the solution for $N_{HD} = 2$ (i.e., with the HDE) yields a sharper WF than those of the standard RE solution (i.e., $N_{HD} = 0$).

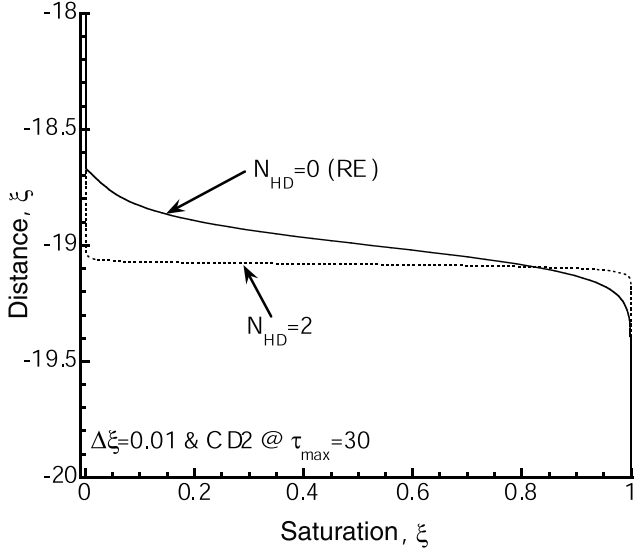


Figure 11. Close-up view of saturation profiles for capillary rise in a vertical domain, subject to constant bottom prescribed pressure, $\Psi_{in} = 0$ at $\xi = -20$. As expected, the wetting front maintains its monotonicity for $N_{HD} = 2$. However, compared to the $N_{HD} = 0$ case (i.e., the RE solution), the HDE solution with $N_{HD} = 2$ yields a sharper WF.

finger tip lengths are within 25%. Thus a value of N_{HD} just above the value where a nonmonotonic response arises in 1D, yields 2D GDF with behavior representative of that found in experiment.

5.2. Nonmonotonicity and Alternative Forms of the HBPU Effect

[35] In this paper and in the work of *Eliassi and Glass* [2002] we have argued that the porous-continuum scale representation of the physics for unsaturated flow must contain a macroscopic HBPU effect to be able to model GDF. As stated by *Eliassi and Glass* [2002], there are a variety of ways to include and mathematically formulate such a HBPU effect. We have focused on approaches that incorporate an additional term in the governing equation. There and in section 1 of this paper, we outlined three possibilities resulting in the HD, hyperbolic and mixed form terms. In this paper we chose to illustrate the HBPU behavior using the HDE, as the HDE did not require any special numerical techniques for its solution. While not presented here, numerical solutions using the hyperbolic form of the HBPU effect also show, similar to the HDE, the required behavior for the porous-continuum simulation of GDF. This is expected because the formulation of the HBPU within the HD and hyperbolic are similar, both include an additional term containing a second derivative (in space for HDE and in time for the hyperbolic). However, our numerical solutions using the mixed form, as formulated in the context of the dynamic capillary pressure of *Hassanizadeh and Gray* [1993a, 1993b], have not yet been shown to yield nonmonotonicity. Indeed, in the work of *Eliassi and Glass* [2002], we could not argue conclusively for a nonmonotonic behavior with the mixed form because it has a spatial-temporal third-order derivative that introduces an additional non-HBPU “swing” across the WF.

[36] As noted by *Eliassi and Glass* [2001a, 2002], nonmonotonicity can also be created through the use of nonstandard constitutive relations or equations of state. Of course, such approaches simply incorporate the same macroscopic HBPU effect in yet another way. We can illustrate this transformation of the HBPU with straightforward manipulation of the HDE. First, to consider a nonstandard constitutive relation, we can rewrite (10) as:

$$\left(\frac{\partial\Theta(\Psi)}{\partial\Psi}\right)\frac{\partial\Psi}{\partial\tau} = \vec{\nabla}^* \cdot [\tilde{\kappa}(\Theta)\vec{\nabla}^*\Psi] + \delta\frac{\partial\kappa(\Theta)}{\partial\xi} \quad (25a)$$

where (25a) is near to the standard form of the RE, except $\tilde{\kappa}(\Theta)$ can be thought of as a “modified permeability function” having the form:

$$\tilde{\kappa}(\Theta) = \kappa(\Theta) \left\{ 1 + N_{HD} \frac{\partial\Lambda}{\partial\Theta} \frac{\partial\Theta}{\partial\Psi} \right\} \quad (25b)$$

Functional variation of $\tilde{\kappa}(\Theta)$ versus saturation is shown Figure 13a, for the same set of N_{HD} values as in Figure 4 (with $n = 15$, $\alpha^* = 1$, and $b = 0.1$). Note that for $N_{HD} = 1$ and smaller, $\tilde{\kappa}(\Theta)$ is always positive and varies near to the standard form of permeability function (i.e., $N_{HD} = 0$ curve). However, for $N_{HD} = 2$ and larger, $\tilde{\kappa}(\Theta)$ becomes nonmonotonic to yield negative values before becoming positive at higher saturation. The functional response of $\tilde{\kappa}(\Theta)$ with respect to the media nonlinearity, n , for the same values as in Figure 9 (with $\alpha^* = 1$, $N_{HD} = 2$, and $b = 0.1$) are shown in Figure 13b. While for $n = 2$ to 9, $\tilde{\kappa}(\Theta)$ is monotonic and is near to standard $\kappa(\Theta)$, for $n = 11$ and above, $\tilde{\kappa}(\Theta)$ is nonmonotonic having a minimum value that is negative. Comparing the presence of nonmonotonicity in $\tilde{\kappa}(\Theta)$ to that found in saturation profiles (Figures 4 and 9), we see a direct correspondence. While negative permeability values are clearly difficult to conceive, $\tilde{\kappa}(\Theta)$ no longer has the same physical meaning as the standard permeability function, especially as N_{HD} increases. However, the ability of $\tilde{\kappa}(\Theta)$ to model nonmonotonic profiles suggests that the standard Darcy flux relation with a nonmonotonic permeability function applied to both capillary and gravity terms, may yield nonmonotonic solutions.

[37] Alternatively, to consider a nonstandard equation of state, we can rewrite (10) as:

$$\left(\frac{\partial\Theta(\Phi)}{\partial\Phi}\right)\frac{\partial\Phi}{\partial\tau} = \vec{\nabla}^* \cdot [\kappa(\Theta)\vec{\nabla}^*\Phi] + \delta\frac{\partial\kappa(\Theta)}{\partial\xi} \quad (26a)$$

where (26a) is again near to the standard form of the RE, except $\Phi(\Theta)$ is a “modified total potential” given by:

$$\Phi = \Phi(\Theta) = \Psi(\Theta) + N_{HD}\Lambda(\Theta) \quad (26b)$$

As (26b) indicates, the modified total potential is comprised of two parts, the first given by the standard equation of state (i.e., $\Psi(\Theta)$) and a second that within the context of the theory of *Hassanizadeh and Gray* [1993a, 1993b], arises from the heat of wetting or the Helmholtz free energy. Figure 14a shows Φ as a function of Θ for the same N_{HD} values as in Figure 4a (with $n = 15$, $\alpha^* = 1$, and $b = 0.1$). While for $N_{HD} < 1$, $\Phi(\Theta)$ is a monotonic function of Θ , as

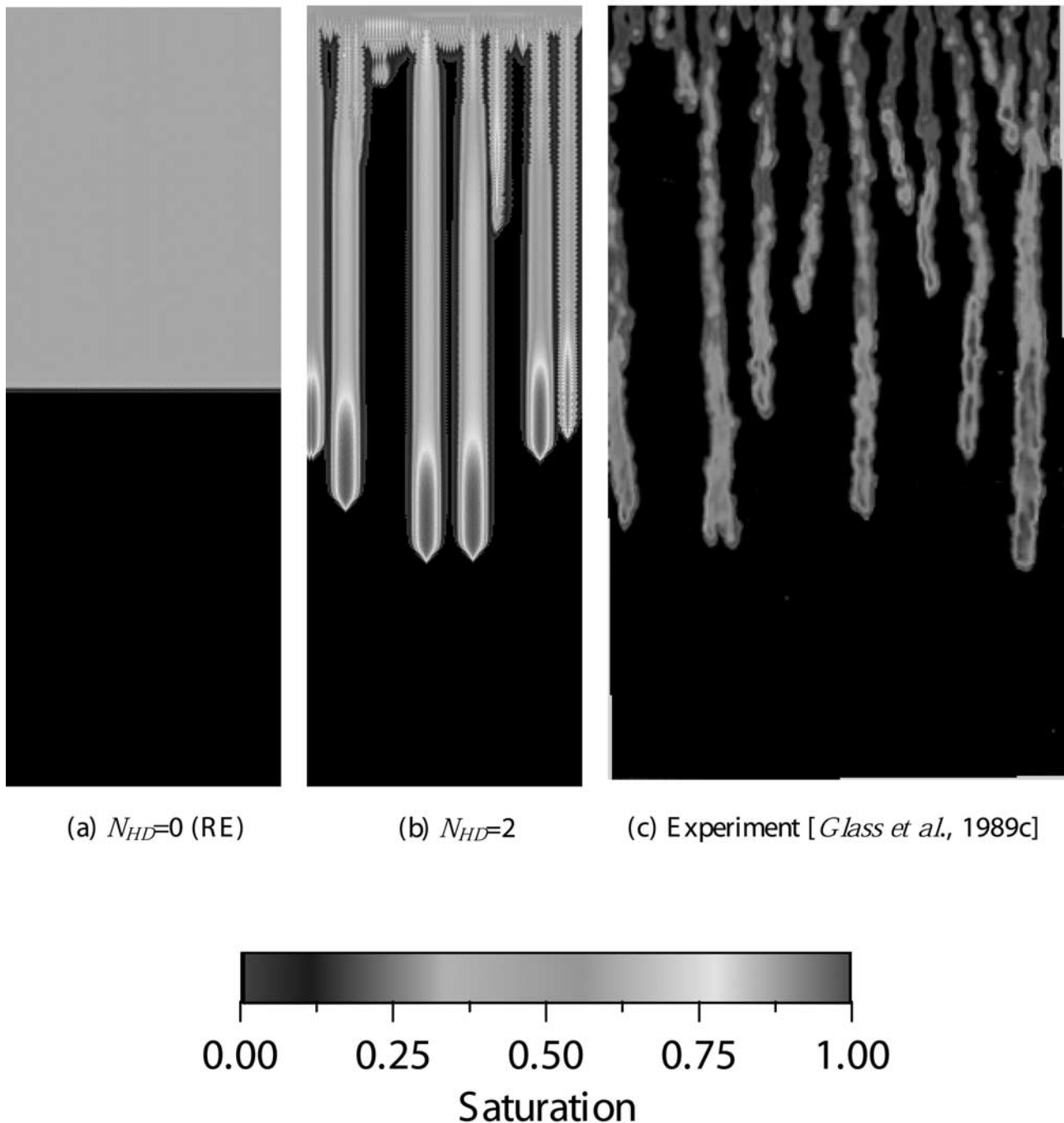
(a) $N_{HD}=0$ (RE)(b) $N_{HD}=2$ (c) Experiment [*Glass et al.*, 1989c]

Figure 12. Portions of the saturation fields for the 2D numerical solutions, using the RE and HDE, are compared with experiment. (a) For $N_{HD} = 0$ (i.e., the standard form of the RE) a uniform and monotonic WF advances into the 2D domain. (b) For $N_{HD} = 2$ the WF breaks up into nonmonotonic GDF. (c) Experimental GDF from *Glass et al.* [1989]. Both numerical solutions (5 by 14.2 dimensionless units) and experiment (8.3 by 14.2 dimensionless units) are shown at the same scale. Dimensionless solution time for both $N_{HD} = 0$ and 2 is $\tau = 30$, which was chosen for comparison with the experiment. Numerical solutions used constant grid spacing of $\Delta\eta = \Delta\xi = 0.03125$ (i.e., 102,400 finite difference nodes, where $\Delta\eta$ is the grid spacing in the η direction) and the CD2 averaging. We emphasize that the 2D numerical solution has not been as exhaustively evaluated as the 1D has, and while we are near, we may not exactly be at the converged (i.e., grid-independent) solution for our $N_{HD} = 2$ case. See color version of this figure at back of this issue.

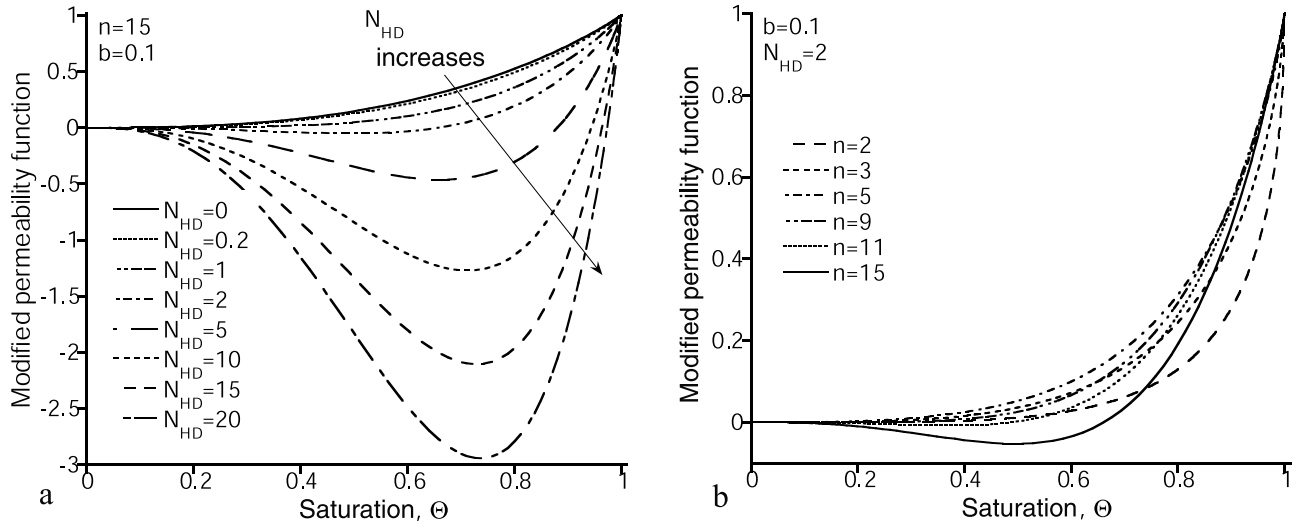


Figure 13. Incorporation of the HBPU into a nonstandard “modified permeability function,” $\tilde{\kappa}(\Theta)$, evaluated using (25b). (a) For a material nonlinearity of $n = 15$, and with the hypodiffusion number of $N_{HD} < 2$, $\tilde{\kappa}(\Theta)$ is a monotonically varying function of saturation, Θ , and behaves near to the standard *Mualem’s* [1976] model (i.e., $N_{HD} = 0$). However, as N_{HD} increases, $\tilde{\kappa}(\Theta)$ becomes nonmonotonic, yielding a negative minimum that depending on N_{HD} , can be quite large. (b) For $N_{HD} = 2$, when n is below 9, $\tilde{\kappa}(\Theta)$ behaves near to that of the standard form (i.e., when $N_{HD} = 0$). However, for n of 11 and larger, $\tilde{\kappa}(\Theta)$ is nonmonotonic. Note that the transition of $\tilde{\kappa}(\Theta)$ from monotonic to nonmonotonic as a function of N_{HD} and n is consistent with a similar transition in the numerical solution of the hypodiffusive governing equation shown in Figures 4 and 9. To evaluate the various parts of (25b), we use (12a), (12b), and (12c) with $\alpha^* = 1$ and $b = 0.1$.

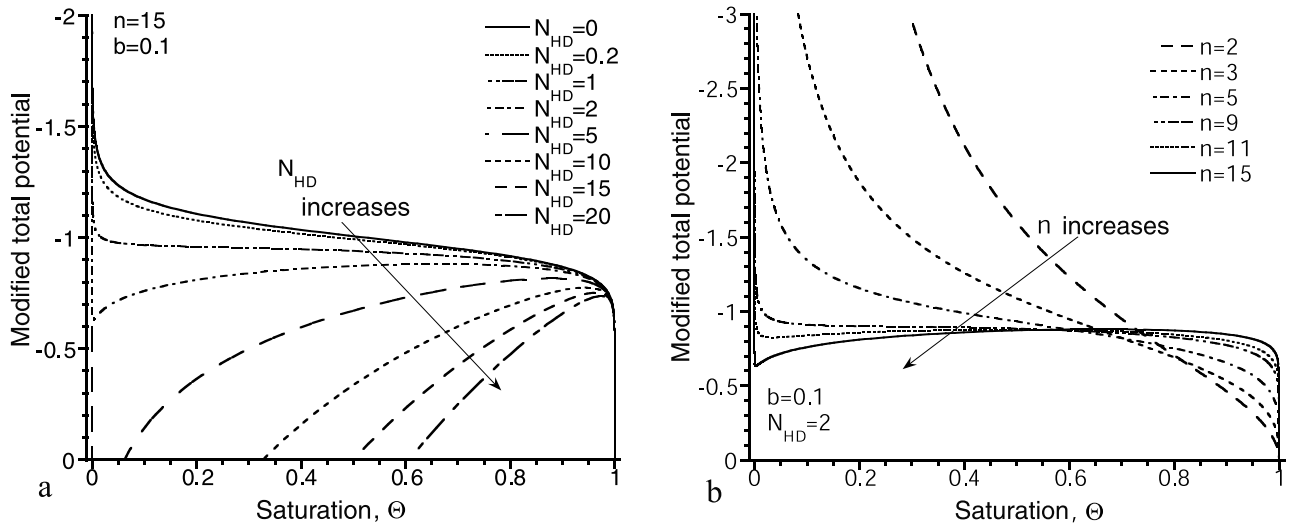


Figure 14. Incorporation of the HBPU into a nonstandard “modified total potential,” $\Phi(\Theta)$, evaluated using (26b). (a) For a material nonlinearity of $n = 15$, while for the hypodiffusion number, $N_{HD} < 2$, $\Phi(\Theta)$ is a monotonic function of saturation and is near to that of the standard *van Genuchten* [1980] model (i.e., $N_{HD} = 0$), for $N_{HD} \geq 2$ the modified total potential is no longer monotonic. For $N_{HD} = 2$, $\Phi(\Theta)$ increases to a value of ~ -0.63 at a saturation of ~ 0.0025 and then begins to decrease until it catches up with the standard model (i.e., $N_{HD} = 0$) as full saturation is approached. While the vertical axis is clipped off at a value of zero, for $N_{HD} = 5$ and larger, $\Phi(\Theta)$ attains maximum values that are positive. (b) For $N_{HD} = 2$ the functional response with respect to the material nonlinearity, n , shows that while for n values of 2 to 9 $\Phi(\Theta)$ is monotonic and near to the standard *van Genuchten* [1980] model; for $n = 11$ and larger, $\Phi(\Theta)$ becomes nonmonotonic. As in Figure 13, the transition of $\Phi(\Theta)$ from monotonic to nonmonotonic as a function of N_{HD} and n also tracks the behavior of the numerical solution results in Figures 4 and 9. To evaluate the various parts of (26b), we use (12a) and (12c) with $\alpha^* = 1$, $b = 0.1$.

N_{HD} increases above 1, $\Phi(\Theta)$ becomes nonmonotonic. Relating the functional behavior of $\Phi(\Theta)$ to that of the saturation profiles (e.g., those shown in Figures 2a, 2c, and 4a), we see that when $\Phi(\Theta)$ becomes nonmonotonic, so do the solutions to the HDE. One can also confirm that for $N_{HD} = 2$, as n is increased to ~ 11 and above, $\Phi(\Theta)$ also becomes nonmonotonic (Figure 14b) as do the solutions shown in Figure 9. Thus we see that the HBPU effect can also be incorporated into a nonmonotonic equation of state.

6. Concluding Remarks

[38] In this paper, we considered the ability of an extended governing equation for porous-continuum scale unsaturated flow to model GDF. As presented by *Eliassi and Glass* [2002], the basis for this governing equation is the experimentally observed hold-back-pile-up (HBPU) effect. The HBPU effect can be mathematically formulated in a variety of ways. In the HDE form that we consider in this paper, the HBPU effect is formulated as a nonlinear Laplacian-type term of the moisture content that is hypodiffusive in nature. While parameterization of a hypodiffusive term is still open, considering the theory of *Gray and Hassanizadeh* [1991], such a term arises by assuming that the free energy of the water phase decreases as a function of saturation. Formulating this function with a simple power law, numerical solution of the 1D form of the HDE (under conditions of constant flux infiltration into initially dry, highly nonlinear, and hysteretic materials), illustrates that the HDE can indeed yield the underlying nonmonotonicity at the WF required by GDF. The behavior of the solution is dependent on the hypodiffusion number, N_{HD} , a new dimensionless group that controls the size of the hypodiffusive term. At small enough values of N_{HD} , the HDE yields a monotonic behavior and the solution is near to the standard form of the RE. As N_{HD} increases, the solution becomes nonmonotonic and the saturation at the 1D “finger tip” increases quickly, yielding a fully saturated tip at an N_{HD} of 2.

[39] Considering an N_{HD} of 2, as we move in parameter space (i.e., initial moisture content, applied flux, and media nonlinearity) out from the region where GDF has been observed, the HDE solution undergoes the required transition to monotonic. Thus, as either the initial moisture content or the applied flux are increased, or the nonlinearity of the porous material, n_{PWC} , is decreased, the nonmonotonic signature of GDF degenerates. We also examined the numerical response of the HDE for a number of situations where the solution must remain monotonic. Examples of such cases include both horizontal imbibition and capillary rise into initially dry and highly nonlinear material. For these examples, monotonicity is indeed found.

[40] Our 1D solutions demonstrate the development of nonmonotonicity as a function of N_{HD} and the critical controls displayed by physical parameters on GDF occurrence. This nonmonotonicity must arise naturally within the governing equation for a porous-continuum approach to be able to model GDF in two and higher dimensions. We illustrate this point in a set of 2D solutions where numerically simulated GDF conforms reasonably well to that found experimentally. Finally, we note that the results found for the HDE, also apply to the alternative hyperbolic formulation of the HBPU effect. Thus one is neither tied to the HDE nor the underlying physics contained within the

theory of *Gray and Hassanizadeh* [1991] to formulate the HBPU effect. Indeed, the HBPU can also be incorporated into an equation of state or even in a constitutive relation. Thus the underlying physics for the HBPU effect, required by a porous-continuum approach to model GDF, remains open.

[41] **Acknowledgments.** This research was supported by the U.S. Department of Energy’s Basic Energy Sciences Geoscience Research Program under contract number DE-AC04-94 AL85000 at Sandia National Laboratories. We wish to express our thanks to S. Majid Hassanizadeh, Antonio del Rio, Norm Roderick, Anil Prinja, Tim Ward, and Bruce Thomson for reviewing an earlier version of this paper and providing many helpful comments. We also wish to thank two anonymous reviewers for their thought provoking comments. Finally, we note that portions of this work were presented at the Fall 2001 American Geophysical Union Meeting [*Eliassi and Glass*, 2001b].

References

- Anderson, D. A., J. C. Tannehill, and R. H. Pletcher, *Computational Fluid Mechanics and Heat Transfer*, Taylor and Francis, Philadelphia, Pa., 1984.
- Celia, M. A., E. T. Bouloutas, and R. L. Zarba, A general mass-conservative numerical solution for the unsaturated flow equation, *Water Resour. Res.*, 26, 1483–1496, 1990.
- del Rio, J. A., and M. Lopez de Haro, A generalization of the Richards equation within extended irreversible thermodynamics, *Water Resour. Res.*, 27, 2141–2142, 1991.
- Diment, G. A., and K. K. Watson, Stability analysis of water movement in unsaturated porous materials: 3. Experimental studies, *Water Resour. Res.*, 21, 979–984, 1985.
- Eliassi, M., On continuum-scale numerical simulations of gravity-driven fingers in unsaturated porous materials, Ph.D. dissertation, Univ. of N. M., Albuquerque, 2001.
- Eliassi, M., and R. J. Glass, On the continuum-scale modeling of gravity-driven fingers in unsaturated porous media: The inadequacy of the Richards equation with standard monotonic constitutive relations and hysteretic equations of state, *Water Resour. Res.*, 37, 2019–2035, 2001a.
- Eliassi, M., and R. J. Glass, Porous continuum-scale modeling of gravity-driven fingers in unsaturated porous materials: Extended flux laws and numerical simulations, *Eos Trans. AGU*, 82(47), Fall Meet. Suppl., abstract H52A-0377, 2001b.
- Eliassi, M., and R. J. Glass, On the porous continuum-scale simulation of gravity-driven fingers in unsaturated materials: Extension of standard theory with an hold-back-pile-up effect, *Water Resour. Res.*, 38(11), 1234, doi:10.1029/2001WR001131, 2002.
- Forsyth, P. A., and M. C. Kropinski, Monotonicity consideration for saturated-unsaturated subsurface flow, *SIAM J. Sci. Comput.*, 18, 1328–1354, 1997.
- Glass, R. J., and M. J. Nicholl, Physics of gravity driven fingering of immiscible fluids within porous media: An overview of current understanding and selected complicating factors, *Geoderma*, 70, 133–163, 1996.
- Glass, R. J., T. S. Steenhuis, and J.-Y. Parlange, Mechanism for finger persistence in homogenous unsaturated, porous media: Theory and verification, *Soil Sci.*, 148, 60–70, 1989.
- Glass, R. J., S. H. Conrad, and W. Peplinski, Gravity-destabilized nonwetting phase invasion in macroheterogeneous porous media: Experimental observations of invasion dynamics and scale analysis, *Water Resour. Res.*, 36, 3121–3138, 2000.
- Gray, W. G., and S. M. Hassanizadeh, Unsaturated flow theory including interfacial phenomena, *Water Resour. Res.*, 27, 1855–1863, 1991.
- Hassanizadeh, S. M., and W. G. Gray, Thermodynamic basis of capillary pressure in porous media, *Water Resour. Res.*, 29, 3389–3406, 1993a.
- Hassanizadeh, S. M., and W. G. Gray, Toward an improved description of the physics of two phase flow, *Adv. Water Resour.*, 16, 53–67, 1993b.
- Haverkamp, R., M. Vauclin, J. Touma, P. J. Wierenga, and G. Vachaud, A comparison of numerical simulation models for one-dimensional infiltration, *Soil Sci. Soc. Am. J.*, 41, 285–294, 1977.
- Liu, Y., T. S. Steenhuis, J. S. Selker, and J.-Y. Parlange, Formation and persistence of fingered flow in coarse grained soils under different moisture contents, *J. Hydrol.*, 159, 187–195, 1994.
- Mualem, Y., A new model for predicting the hydraulic conductivity of unsaturated porous media, *Water Resour. Res.*, 12, 513–522, 1976.

- Ozisik, N., *Heat Conduction*, John Wiley, New York, 1980.
- Scott, P. S., G. J. Farquhar, N. Kouwen, Hysteretic effects on net infiltration, in *Advances in Infiltration, ASAE Publ. 11-83*, pp. 163–170, Am. Soc. of Agric. Eng., St. Joseph, Mich., 1983.
- Selker, J. S., J.-Y. Parlange, and T. S. Steenhuis, Fingering flow in two dimensions: 2. Predicting finger moisture profile, *Water Resour. Res.*, 28, 2523–2528, 1992.
- Sililo, O. T. N., and J. H. Tellam, Fingering in unsaturated zone flow: A qualitative review with laboratory experiments in heterogeneous systems, *Ground Water*, 38, 864–871, 2000.
- van Genuchten, M. T., A closed-form equation for predicting the hydraulic properties of unsaturated soils, *Soil Sci. Soc. Am. J.*, 44, 892–898, 1980.
- Yao, T. M., and J. M. H. Hendrickx, Stability of wetting fronts in dry homogenous soils under low infiltration rates, *Soil Sci. Soc. Am. J.*, 60, 20–28, 1996.

M. Eliassi and R. J. Glass, Flow Visualization and Processes Laboratory, Sandia National Laboratories, Albuquerque, NM 87185-0735, USA. (meliassi@sandia.gov; rjglass@sandia.gov)

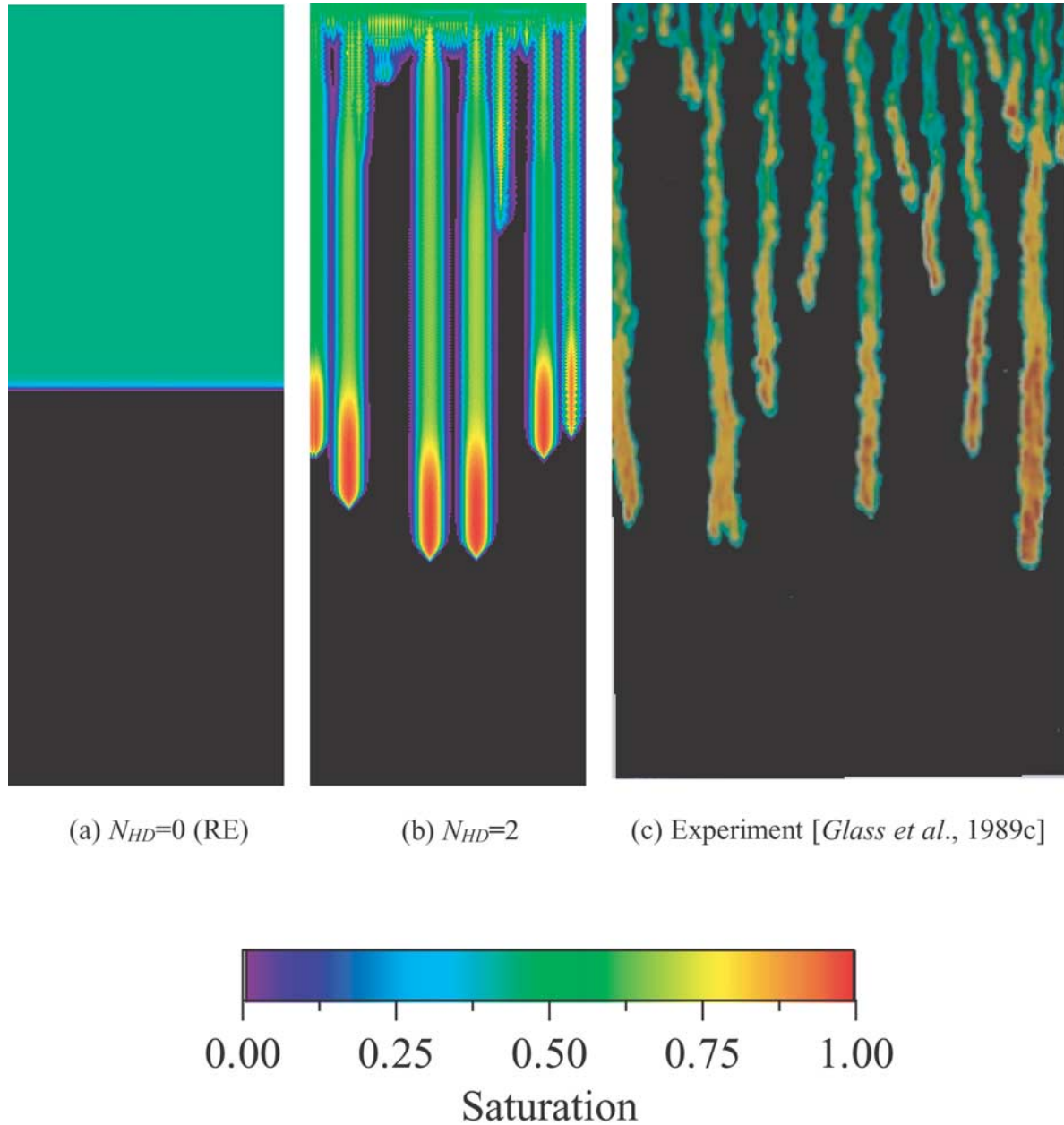


Figure 12. Portions of the saturation fields for the 2D numerical solutions, using the RE and HDE, are compared with experiment. (a) For $N_{HD} = 0$ (i.e., the standard form of the RE) a uniform and monotonic WF advances into the 2D domain. (b) For $N_{HD} = 2$ the WF breaks up into nonmonotonic GDF. (c) Experimental GDF from Glass *et al.* [1989]. Both numerical solutions (5 by 14.2 dimensionless units) and experiment (8.3 by 14.2 dimensionless units) are shown at the same scale. Dimensionless solution time for both $N_{HD} = 0$ and 2 is $\tau = 30$, which was chosen for comparison with the experiment. Numerical solutions used constant grid spacing of $\Delta\eta = \Delta\xi = 0.03125$ (i.e., 102,400 finite difference nodes, where $\Delta\eta$ is the grid spacing in the η direction) and the CD2 averaging. We emphasize that the 2D numerical solution has not been as exhaustively evaluated as the 1D has, and while we are near, we may not exactly be at the converged (i.e., grid-independent) solution for our $N_{HD} = 2$ case.